A global atmospheric model of meteoric iron

Wuhu Feng,[1,2] Daniel R. Marsh,[3] Martyn P. Chipperfield,[2] Diego Janches,[4]
Josef Höffner,[5] Fan Yi,[6] and John M. C. Plane[1]

Received 19 February 2013; revised 1 August 2013; accepted 2 August 2013; published 29 August 2013.

[1] The first global model of meteoric iron in the atmosphere (WACCM-Fe) has been developed by combining three components: the Whole Atmosphere Community Climate Model (WACCM), a description of the neutral and ion-molecule chemistry of iron in the mesosphere and lower thermosphere (MLT), and a treatment of the injection of meteoric constituents into the atmosphere. The iron chemistry treats seven neutral and four ionized iron containing species with 30 neutral and ion-molecule reactions. The meteoric input function (MIF), which describes the injection of Fe as a function of height, latitude, and day, is precalculated from an astronomical model coupled to a chemical meteoric ablation model (CABMOD). This newly developed WACCM-Fe model has been evaluated against a number of available ground-based lidar observations and performs well in simulating the mesospheric atomic Fe layer. The model reproduces the strong positive correlation of temperature and Fe density around the Fe layer peak and the large anticorrelation around 100 km. The diurnal tide has a significant effect in the middle of the layer, and the model also captures well the observed seasonal variations. However, the model overestimates the peak Fe^+ concentration compared with the limited rocket-borne mass spectrometer data available, although good agreement on the ion layer underside can be obtained by adjusting the rate coefficients for dissociative recombination of Fe-molecular ions with electrons. Sensitivity experiments with the same chemistry in a 1-D model are used to highlight significant remaining uncertainties in reaction rate coefficients, and to explore the dependence of the total Fe abundance on the MIF and rate of vertical transport.

Citation: Feng, W., D. R. Marsh, M. P. Chipperfield, D. Janches, J. Höffner, F. Yi, and J. M. C. Plane (2013), A global atmospheric model of meteoric iron, *J. Geophys. Res. Atmos.*, *118*, 9456–9474, doi:10.1002/jgrd.50708.

1. Introduction

[2] The mesosphere lower thermosphere (MLT) region (∼60–120 km) connects the atmosphere below with space above and is a region of increasing scientific and practical interest, because this region is affected by solar variability and climate change. One unique feature in the MLT is the presence of layers of metal neutral and ionized atoms. However, it is only possible to make in situ measurements in the MLT using rocket-borne instruments, so that most knowledge of the region has been gained by remote sensing. The ablation of meteoroids in the MLT is the source of the layers of metal atoms such as Fe and Na, which occur globally between 80 and 105 km. These metal atoms can be monitored by ground-based resonance lidars, providing tracers of physics (winds, gravity waves, tides, and temperature) and photochemistry with unrivaled temporal and spatial resolution [*Plane*, 2003]. The metal layers can also be observed with UV-visible spectrometers on satellites [*Fan et al.*, 2007; *Scharringhausen et al.*, 2008; *Fussen et al.*, 2010; *Hedin and Gumbel*, 2011] providing near-global coverage. The metal layers thus offer a unique way to understand the coupling of atmospheric chemistry and dynamical processes, as well as testing the accuracy of climate models in the MLT (D. R. Marsh D. Janches, W. Feng, and J. M. C. Plane, A global model of meteoric sodium, submitted to *Journal Geophysical Research Atmospheres*, 2013, hereinafter referred to as Marsh et al., submitted manuscript, 2013).

[3] Previously, modeling studies of the mesospheric metal layers have employed 1-D models to investigate the chemistry controlling the metal layers [e.g., *Plane*, 2003; *Plane and Whalley*, 2012]. These models are useful for optimizing detailed neutral and ion-molecule chemistry schemes, where not all the relevant rate coefficients have been measured in the laboratory under mesospheric conditions. The

[1]School of Chemistry, University of Leeds, Leeds, UK.
[2]NCAS, School of Earth and Environment, University of Leeds, Leeds, UK.
[3]National Center for Atmospheric Research, Boulder, Colorado, USA.
[4]Space Weather Laboratory, NASA Goddard Space Flight Center, Greenbelt, Maryland, USA.
[5]Leibniz Institute of Atmospheric Physics, Kühlungsborn, Germany.
[6]School of Electronic Information, Wuhan University, Wuhan, China.

Corresponding author: J. M. C. Plane, School of Chemistry, University of Leeds, Leeds, LS2 9JT, UK. (j.m.c.plane@leeds.ac.uk)

2169-897X/13/10.1002/jgrd.50708

Table 1. Ground-Based Stations With Atomic Fe Measurements by Lidar

Station	Latitude	Longitude	Period	Reference
Urbana	40°N	272°E	1995–1996	*Helmer et al.* [1998]
Wuhan	30°N	114°E	2001–2003	*Yi et al.* [2009]
Rothera	68°S	292°E	2003–2005	*Gardner et al.* [2011]
Davis	69°S	78°E	2010–2011	*Lübken et al.* [2011]
South Pole	90°S		1999–2000	*Gardner et al.* [2001]

model output is typically compared to lidar observations at a single observing location. This approach has been reasonably successful, since the removal lifetime of a metal atom from its layer is relatively short (typically a few days) because of the high rate of vertical transport by eddy and molecular diffusion [*Plane*, 2004]. The removal lifetime is much longer than the chemical turnover lifetime, which is comparatively short (a few seconds) because of rapid recycling between the metal atoms (e.g., Fe) and their oxides (e.g., FeO) by reactions with O_3 and O, respectively. It should be noted that mesospheric metal layers are very narrow (a few kilometers wide), with small topside and bottomside scale heights because of rapid vertical changes in the ion-molecule and neutral chemistry, respectively. The layers are also very responsive to dynamical process such as gravity waves and tides.

[4] However, a 1-D model is not able to resolve the large-scale horizontal distribution of the metallic species, which is affected by many important MLT processes: tidal propagation is important in determining winds structure in the MLT region [*Pancheva et al.*, 2002]; the injection of the metal species by meteoric ablation, which varies with latitude and season [*Janches et al.*, 2006]; rapid meridional transport (e.g., a study of the Na and Fe layers at South Pole [*Gardner et al.*, 2005] identified the importance of convergence of the meridional circulation over the pole during winter in explaining the unusually high wintertime concentrations of Fe and Na); the effect on metal chemistry of photochemical species like O and H; and the role of polar mesospheric clouds which occur at high latitudes during summer [*Plane et al.*, 2004]. A 3-D global model is therefore required to gain a complete picture of the metal layers in the MLT, and to compare with the growing database of measurements made by lidars and satellites.

[5] In this paper we describe the addition of a complete Fe chemistry module into the Whole Atmosphere Community Climate Model (WACCM). This complements a parallel study of the global mesospheric Na layer (Marsh et al., submitted manuscript, 2013). Different metals have different chemistries which control the characteristic features of their layers. There are several reasons for a focus on Fe. First, Fe is the most abundant metal in the MLT [*Plane*, 2003]: the peak abundance in the Fe layer is 2–3 times larger than for Na [*Helmer et al.*, 1998; *Gardner et al.*, 2005]. Second, because Fe is less volatile than Na, it is injected through meteoric ablation about 12 km lower in the MLT than Na [*Vondrak et al.*, 2008]. The resulting atomic Fe peak is several kilometers lower than Na with a smaller bottomside scale height [*Plane*, 2003]. Third, there are uncertainties in the size and velocity distributions of the interplanetary dust particles entering the atmosphere, so that the relative Fe and Na injection rates, as well as their absolute values, are quite uncertain [*Plane*, 2012]. Investigating different MLT metal layers within the same model will thus allow us to better understand the astronomy, chemistry, and transport processes that control the different metal layers in the MLT.

[6] Section 2 of the paper contains a brief description of the lidar measurements and rocket data we have used to evaluate the model. We then describe in section 3 the new WACCM-Fe model, which is based on three components: a whole atmosphere community climate model; the neutral and ion-molecule iron chemistry in the MLT; and the injection of meteoric constituents into the atmosphere. The model results are presented in section 4, including comparisons with observations and some sensitivity analyses using a 1-D model with the same chemistry. Section 5 contains our conclusions.

2. Ground-Based Lidar and Rocket-Borne Mass Spectrometric Measurements

[7] Table 1 lists the ground-based lidar Fe data which we have used to evaluate WACCM-Fe: two stations at NH midlatitudes (Urbana, U.S., and Wuhan, China) and three southern hemisphere (SH) high-latitude stations (Rothera, Davis, and South Pole in Antarctica). The monthly mean Fe density data at 30°N used here is calculated from nighttime lidar measurements at Wuhan (30.5°N, 114.4°E) from March 2004 to December 2008 [*Yi et al.*, 2009]. Since these data are unpublished, a brief description follows. The raw Fe lidar data were collected with an altitude resolution of 96 m and a time resolution of 5 min. The Fe density profiles were derived from the corresponding lidar photon count profiles by using a standard inversion method [*Gardner*, 1989]. The normalization altitude was set to 30 km, and the number density value of air molecules at this altitude was taken from radiosonde observations at a local weather station. The absolute accuracies of the nightly mean Fe density profiles are generally limited to ±8% by the seasonal and diurnal variations in the calibration density [*Yi et al.*, 2009]. For obtaining the main Fe layer without contamination from sporadic events, those profiles containing sporadic Fe layers were excluded. The remaining data represent 590 h of Fe measurements on 82 different nights during 4 years. The monthly mean Fe profiles were obtained by averaging the nightly means. The Fe lidar over Davis station is a two-wavelength system. Fe density, Doppler temperature, and vertical winds are measured by the Doppler broadening and shift of the iron resonance line at 386 nm [*Höffner and Lautenbach*, 2009]. Nearly background-free observations during day and night are achieved by using a small field of view of 65 μrad together with narrow band filtering by a double etalon at 386 nm [*Höffner and Lautenbach*, 2009]. It should be mentioned that there are other lidar Fe observations [e.g., *Alpers et al.*, 1990, 1994; *Raizada and Tepley*, 2003; *Chu et al.*, 2011a, 2011b], which have not been included in this study.

Table 2. Rocket-Borne Mass Spectrometric Measurements of Fe^+

Payload	Latitude	Longitude	Date[a]	Time (UTC)	Reference
18.1020	51°N	267°E	24/02/1979	16:52	*Kopp* [1984]
S37	68°N	22°E	03/08/1982	23:32	*Kopp* [1984]
S261	68°N	22°E	30/07/1978	23:33	*Kopp et al.* [1985]
S262	68°N	22°E	13/08/1978	23:18	*Kopp et al.* [1985]

[a]Dates are formatted as day/month/year.

Table 3. Iron Photolysis Chemistry Added Into WACCM

No.	Reaction	Rate / (s^{-1})	Reference
J1	$FeOH + h\nu \rightarrow Fe + OH$	$j_1 = 1 \times 10^{-5}$	
J2	$Fe + h\nu \rightarrow Fe^+ + e^-$	$j_2 = 5 \times 10^{-7}$	*Bautista et al.* [1998]

[8] Fe neutral atoms can be converted to ions (Fe^+) by charge transfer reactions with NO^+ and O_2^+ [e.g., *Plane*, 2003; *Saran et al.*, 2011]. Table 2 describes the set of Fe^+ measurements made using mass spectrometry on sounding rockets, which we have used for this study [*Kopp*, 1984; *Kopp et al.*, 1985]. The table lists a number of NH rocket flights, mainly at high latitudes, during both day and night. Rocket-borne measurements have also been made by other groups [e.g., *Grebowsky and Aikin*, 2002; *Roddy et al.*, 2004]. It should be noted that Fe^+ profiles can vary significantly between rocket flights because of the electrodynamical forces which affect the ion distribution and operate in addition to the dynamical forces which also affect neutral species [*Kopp*, 1997]. Global measurements of Fe and Fe^+ using satellite-borne spectrometers operating in the near-UV have not yet been reported.

3. Model Description

[9] WACCM is a comprehensive numerical model extending vertically from the surface to about 140 km [*Garcia et al.*, 2007; *Marsh et al.*, 2007; 2013]. It uses the NCAR Community Earth System Model (CESM) as a common numerical framework [*Hurrel et al.*, 2013]. Here we used WACCM version 4 (cesm1.0.3), which has a hybrid σ-pressure vertical coordinate with 88 levels ($1000 - 5.96 \times 10^{-6}$ hPa). The vertical resolution in the MLT is about 3.5 km. The horizontal resolution is 1.9° (in latitude) × 2.5° (in longitude). The model has a very detailed description of mesospheric and lower thermosphere processes, including nonlocal thermodynamic equilibrium, radiative transfer, auroral processes, ion drag, and molecular diffusion of major and minor species and an interactive chemistry module, thereby resolving most known neutral chemistry and major ion chemistry in the middle and upper atmosphere [*Marsh et al.*, 2007; *Liu et al.*, 2010]. There are parameterizations for other key processes (e.g., gravity waves, heterogeneous chemical processes, the solar cycle, and solar proton events).

[10] WACCM also has an option to perform numerical atmospheric simulations with specified dynamics using the Goddard Earth Observing System 5 (GEOS5) meteorological data set (e.g., temperature, specific humidity, horizontal winds) below 60 km [*Marsh*, 2011; *Lamarque et al.*, 2012; Marsh et al., submitted manuscript, 2013]. Here we take the same nudging coefficient value (0.01) when assimilating the GEOS5 analysis into WACCM (the so-called specified dynamics WACCM or SD-WACCM). This means that 1% of the meteorological conditions (i.e., temperature, winds, surface pressure, specific humidity, surface wind stress, latent, sensible heat flux, etc.) are combined with WACCM fields below 60 km at every model dynamics time step. Above 60 km there is no nudging to the reanalysis fields and the model in this region is free-running.

[11] Although the interaction between polar mesospheric clouds (PMCs) and sodium species was not included in our recent study of the Na layer (Marsh et al., submitted manuscript, 2013), the Fe peak layer is about 5 km lower than the observed Na peak layer [e.g., *Plane*, 2003; *Chen and Yi*, 2011; *Yue et al.*, 2013] in the MLT, and the Fe layer is substantially depleted at PMC altitudes during the polar summer season [*Plane et al.*, 2004]. Therefore, it is crucial to consider PMC interactions in the model. Here we include the PMC microphysics parameterization from *Merkel et al.* [2009] to specify the PMC volumetric surface area (VSA_{pmc}). VSA_{pmc} is calculated using the ice particle radius, which is parameterized in terms of ice water content (IWC) and temperature in WACCM [*Merkel et al.*, 2009].

3.1. Mesospheric Iron Chemistry

[12] Tables 3–5 list the Fe chemical reactions and their rate coefficients which were added to WACCM. Inspection of Tables 3 and 4 shows that many of the rate coefficients for the neutral and ion-molecule reactions have now been measured in the laboratory under mesospheric conditions. Previous modeling studies [e.g., *Helmer et al.*, 1998; *Plane et al.*, 2003], which only looked at the nighttime Fe layer, did not include photochemical reactions. Here we include

Table 4. Neutral Chemistry of Iron Added Into WACCM

No.	Reaction	Rate / ($cm^3 molecule^{-1} s^{-1}$)	Reference
R1	$Fe + O_3 \rightarrow FeO + O_2$	$k_1 = 2.94 \times 10^{-10} \exp(-174/T)$	*Helmer et al.* [1998]
R2	$FeO + O \rightarrow Fe + O_2$	$k_2 = 4.6 \times 10^{-10} \exp(-350/T)$	*Self and Plane* [2003]
R3	$FeO + O_3 \rightarrow FeO_2 + O_2$	$k_3 = 3.0 \times 10^{-10} \exp(-177/T)$	*Rollason and Plane* [2000]
R4	$FeO + O_2 + M \rightarrow FeO_3 + M$	$k_4 = 4.41 \times 10^{-30} \exp(T/200)^{0.606}$	*Rollason and Plane* [2000]
R5	$FeO_2 + O \rightarrow FeO + O_2$	$k_5 = 1.4 \times 10^{-10} \exp(-580/T)$	*Self and Plane* [2003]
R6	$FeO_2 + O_3 \rightarrow FeO_3 + O_2$	$k_6 = 4.4 \times 10^{-10} \exp(-170/T)$	*Self and Plane* [2003]
R7	$FeO_3 + O \rightarrow FeO_2 + O_2$	$k_7 = 2.3 \times 10^{-10} \exp(-2310/T)$	*Self and Plane* [2003]
R8	$FeO_3 + H_2O \rightarrow Fe(OH)_2 + O_2$	$k_8 = 5.0 \times 10^{-12}$	*Self and Plane* [2003]
R9	$FeO + H_2O + M \rightarrow Fe(OH)_2 + M$	$k_9 = 5 \times 10^{-28} \exp(200/T)^{1.13}$	*Rollason and Plane* [2000]
R10	$Fe(OH)_2 + H \rightarrow FeOH + H_2O$	$k_{10} = 3.3 \times 10^{-10} \exp(-302/T)$	*Jensen and Jones* [1974]
R11	$FeO_3 + H \rightarrow FeOH + O_2$	$k_{11} = 3 \times 10^{-10} \exp(-796/T)$	*Plane et al.* [1999]
R12	$FeOH + H \rightarrow Fe + H_2O$	$k_{12} = 3 \times 10^{-10} \exp(-1264/T)$	*Plane et al.* [1999]
R13	$FeOH + FeOH \rightarrow (FeOH)_2$	$k_{13} = 9.0 \times 10^{-10}$	
R14	$Fe \rightarrow FePMC$	$k_{14} = 4.86\ T^{0.5} VSA_{pmc}$	
R15	$FeOH \rightarrow FePMC$	$k_{15} = 4.26\ T^{0.5} VSA_{pmc}$	
R16	$Fe(OH)_2 \rightarrow FePMC$	$k_{16} = 3.83\ T^{0.5} VSA_{pmc}$	
R17	$FeO_3 \rightarrow FePMC$	$k_{17} = 3.57\ T^{0.5} VSA_{pmc}$	
R18	$FePMC \rightarrow FeOH$	0	

Table 5. Ion-Molecule Chemistry of Iron Added Into WACCM

No.	Reaction	Rate / (cm^3 $molecule^{-1}$ s^{-1})	Reference
R19	$Fe^+ \rightarrow$ FePMC	$k_{19} = 4.86T^{0.5} VSA_{pmc}$	
R20	$Fe^+ + O_3 \rightarrow FeO^+ + O_2$	$k_{20} = 7.6 \times 10^{-10}\exp(-240.5/T)$	*Rollason and Plane* [2000]
R21	$FeO^+ + O \rightarrow Fe^+ + O_2$	$k_{21} = 3 \times 10^{-11}$	*Woodcock et al.* [2006]
R22	$Fe^+ + N_2 + M \rightarrow FeN_2^+ + M$	$k_{22} = 4 \times 10^{-30}(T/300.)^{-1.52}$	*Vondrak et al.* [2006]
R23	$Fe^+ + O_2 + M \rightarrow FeO_2^+ + M$	$k_{23} = 8.3 \times 10^{-30}(T/300.)^{-1.86}$	*Vondrak et al.* [2006]
R24a	$FeN_2^+ + O \rightarrow FeO^+ + N_2$	$k_{24a} = 5 \times 10^{-11}$	*Rollason and Plane* [1998]
R24b	$FeO_2^+ + O \rightarrow FeO^+ + O_2$	$k_{24b} = 5 \times 10^{-11}$	*Rollason and Plane* [1998]
R25	$Fe^+ + e^- \rightarrow Fe + h\nu$	$k_{25} = 6.5 \times 10^{-12}(T/300)^{-0.51}$	*Nahar et al.* [1997]
R26	$Fe + O_2^+ \rightarrow Fe^+ + O_2$	$k_{26} = 1.1 \times 10^{-9}$	*Rutherford and Vroom* [1972]
R27	$Fe + NO^+ \rightarrow Fe^+ + NO$	$k_{27} = 9.2 \times 10^{-10}$	*Rutherford and Vroom* [1972]
R28a	$FeO^+ + e^- \rightarrow Fe + O$	$k_{28a} = 3 \times 10^{-7} \sqrt{200./T}$	*Plane et al.* [1999]
R28b	$FeO_2^+ + e^- \rightarrow Fe + O_2$	$k_{28b} = 3 \times 10^{-7} \sqrt{200./T}$	*Plane et al.* [1999]

the photo-ionization of Fe, which is calculated using high-level electronic structure calculations [*Bautista et al.*, 1998]. Following a laboratory study which showed that FeOH is likely to be the major Fe reservoir immediately below the Fe layer [*Self and Plane*, 2003], we have included its photolysis. However, since the FeOH bond energy is around 350 kJ mol^{-1} [*Hastie*, 1990], this molecule will not photolyse until well into the UV, and we have assigned it a small photodissociation rate coefficient compared with that of NaOH, which has been measured [*Self and Plane*, 2002].

[13] One of the important loss processes for the metal layers is the loss of iron-containing molecules on meteoric smoke particles (MSPs) [*Plane*, 2004], which have been observed through a number of independent techniques including the first global measurements using optical extinction with the SOFIE instrument on the AIM satellite [*Hervig et al.*, 2009a, 2009b]. Although we plan in a future version of the model to incorporate explicitly the formation of MSPs from the polymerization of Fe-Mg-Na-Si-O compounds, here the uptake of FeOH, the major Fe reservoir below the Fe peak, on MSPs is treated as a dimerization reaction. The dipole moment of FeOH is 2.7 debye, calculated for the lowest-lying quartet electronic state at the B3LYP/6-311+g(2d,p) level of theory using the Gaussian 09 program [*Frisch et al.*, 2009]. The dimerization rate coefficient (reaction 13 in Table 4) is then set to the dipole-dipole capture frequency [*Maitland et al.*, 1987], increased by a factor of 2 to allow for the polymerization of FeOH with Mg, Na, and Si reservoir compounds. *Plane* [2004] showed that this was equivalent to an uptake on a population of smoke particles. The uptake coefficients of various Fe species on PMCs are set to 1 (reactions 14–17 in Table 4 and reaction 19 in Table 5), based on a laboratory study of the uptake of Fe on low-temperature ice [*Murray and Plane*, 2003]. Reaction 18 in Table 4 allows for the evaporation of Fe species in PMC ice particles when the particles sublimate. For the model runs shown here, this process was turned off following the observation that Fe atoms do not desorb with H_2O molecules at a temperature of 150 K, which was found in a laboratory experiment involving the temperature-programmed desorption of water ice on which Fe had been deposited (V. L. Frankland, University of Leeds, personal communication, 2012). Presumably in the MLT the metal-containing molecules which have adhered to the ice particle will coat the original meteoric smoke particles (or other ice nuclei) on which H_2O molecules are condensed, so that a residue of refractory material remains behind as a coalesced particle. The net effect of this will be to speed up the condensation and coagulation of meteor smoke.

3.2. Meteoric Input Function

[14] An astronomical model of meteoroid fluxes [*Fentzke and Janches*, 2008] is combined with the Chemical Ablation Model CABMOD [*Vondrak et al.*, 2008] to provide the meteoric input function (MIF) for the injection rates of Fe atom into the atmosphere as a function of height, season, and latitude. (Marsh et al., submitted manuscript, 2013) provide details of how both models are coupled to obtain the MIF.

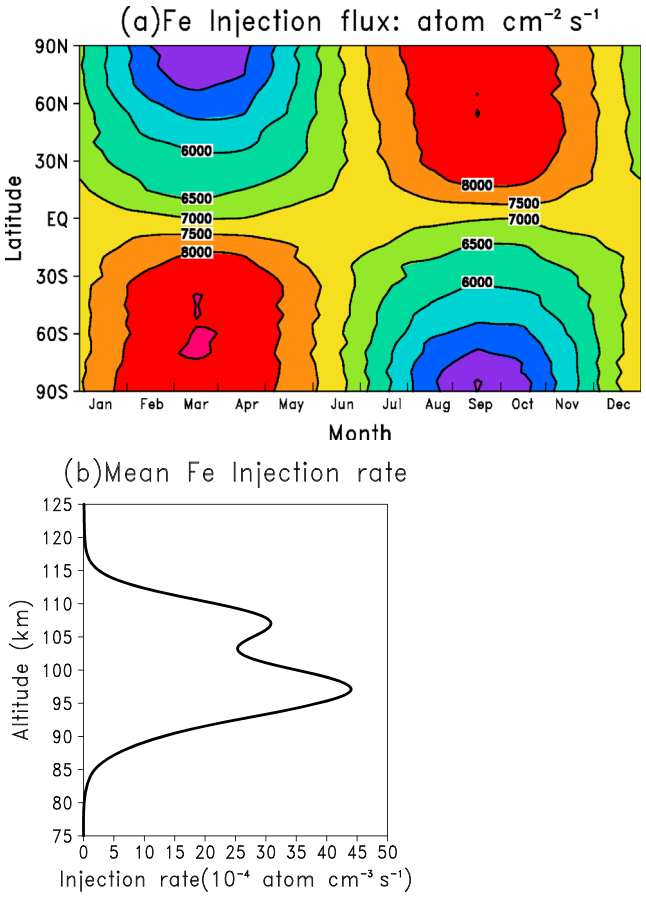

Figure 1. (a) Seasonal varying meteoric Fe column input function (cm^{-2} s^{-1}) and (b) global annual mean Fe injection rate (cm^{-3} s^{-1}) used in WACCM.

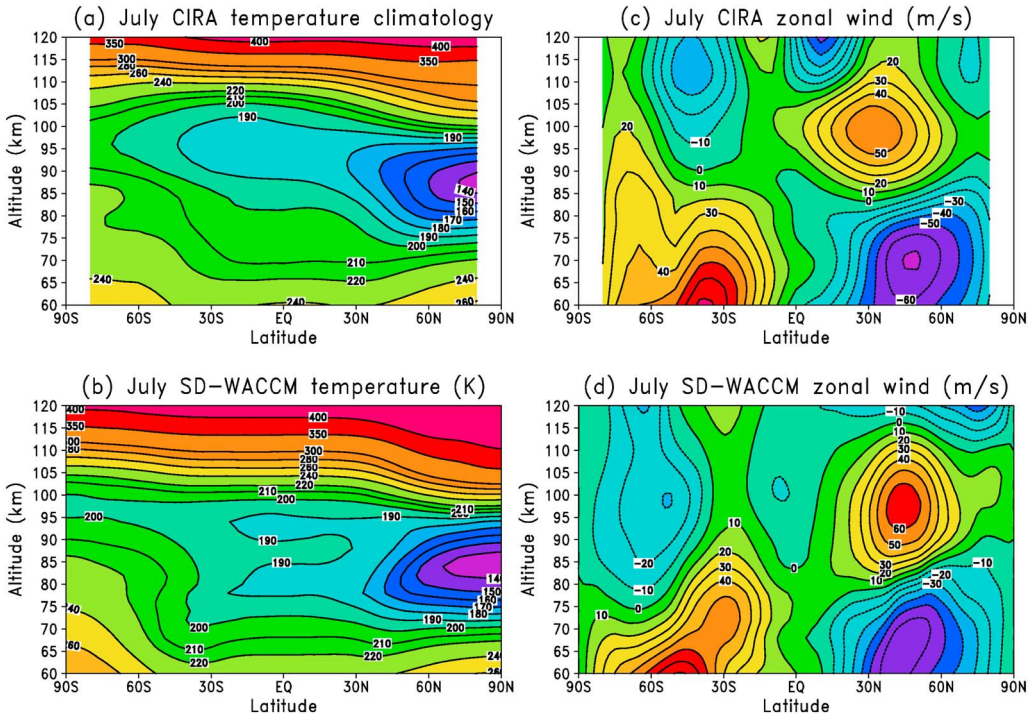

Figure 2. Comparison of the July (a,b) zonal mean temperature (K) and (c,d) zonal wind (m s^{-1}) from the archived CIRA climatology and the SD-WACCM model (averaged from 2005 to 2011).

Briefly, they initially use current knowledge of the astronomical characteristics of the Sporadic Meteor Complex to estimate the global meteoric mass flux into the Earth's upper atmosphere. Their first-time model determines the meteoric mass which is deposited within a small volume in the MLT at all latitudes and days of the year, thus addressing the seasonal and geographical variability of meteoroid masses in the size range of 10^{-8} to 10^{3} μg, which represents the major contributors of metals in the upper atmosphere [*Ceplecha et al.*, 1998]. The simulation assumes that this input originates from the six main sporadic meteoroid populations (i.e., 33% of the meteors are assigned to the Apex, 22% to the Helion, 22% to the Anti-Helion, 11.5% to the North Toroidal, and 11.5% to the South Toroidal) and assign their characteristics (i.e., velocity, diurnal variability, and entry angle) accordingly. This enables the time evolution of the population's incoming angular and velocity characteristics in a given geographical location to be determined.

[15] CABMOD was then used to prepare a look-up table containing the ablation profiles of each metallic element as a function of meteoroid mass (10^{-8} to 10^{3} μg), velocity (11 to 72 km s^{-1}) and entry angle with respect to the zenith (0 to 90°). The extraterrestrial material is assumed to have a CI chondrite composition [*Vondrak et al.*, 2008]. The respective resolutions of the table were 10 divisions per decade of mass, 5 km s^{-1}, and 5°). Interpolation was then used to determine the ablation profile for each individual meteoroid resulting from the astronomical model. The integrated injection rate of Fe as a function of time and place was then calculated by integrating over the meteor population.

[16] Figure 1 shows the resulting Fe column injection rate as a function of latitude and time of year. There is a minimum in the MIF at high latitudes in spring (i.e., February to April in the NH and September to October in the SH)

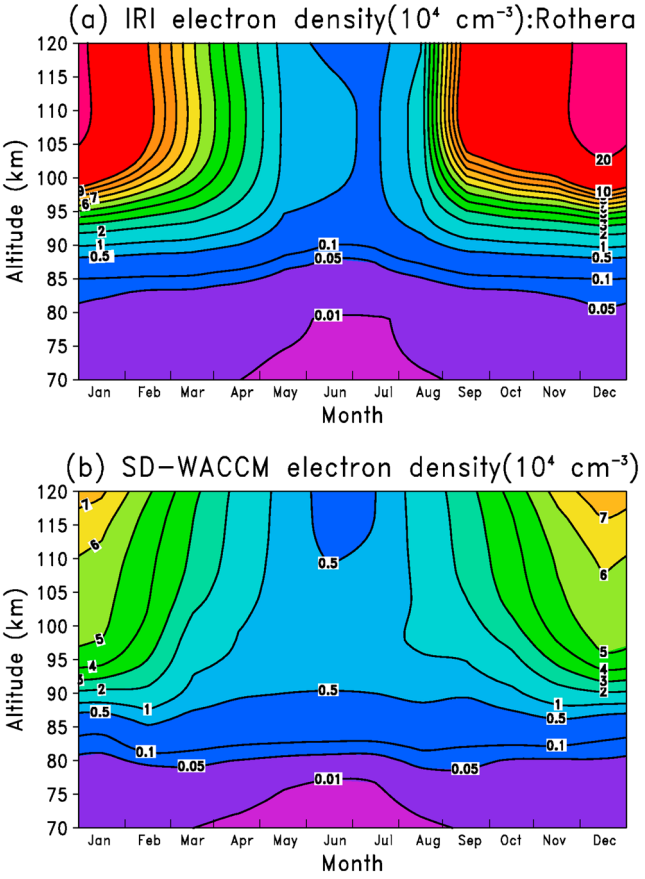

Figure 3. Comparison of the electron density calculated by the (a) IRI and (b) SD-WACCM models, for Rothera.

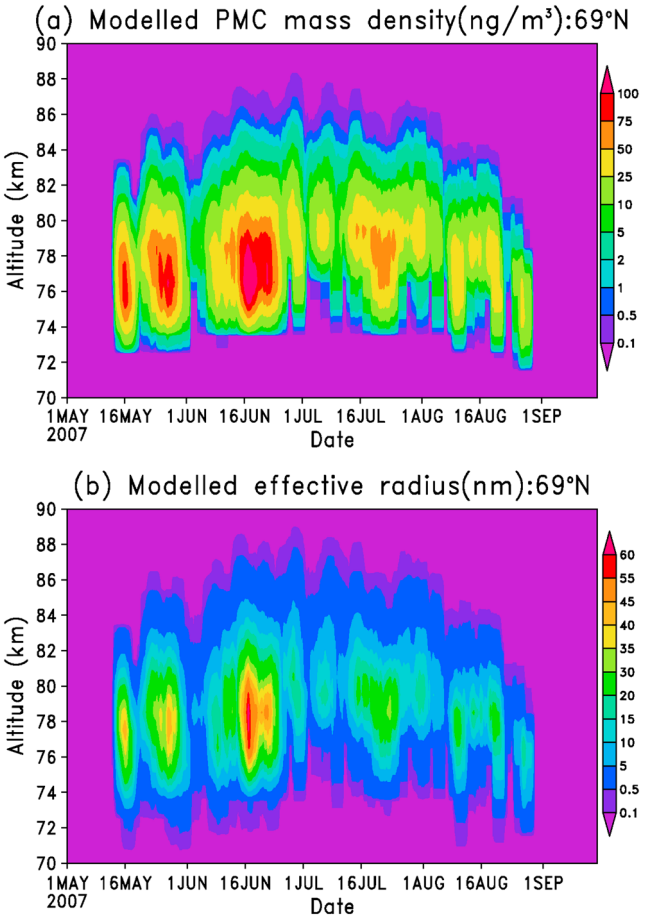

Figure 4. Time series of (a) modeled ice mass and (b) effective radius as a function of altitude for 69°N.

with ~5000 atoms cm^{-2} s^{-1}, and a maximum in autumn (i.e., September to October in the NH and February to April in SH) with ~8500 atoms cm^{-2} s^{-1}. The annual mean Fe MIF is 7080 atoms cm^{-2} s^{-1}. Figure 1 also shows the vertical profile of the global annual mean Fe injection rate. This peaks at 97 km with a value of 0.0045 atoms cm^{-3} s^{-1}; there is a secondary peak at 107 km produced by the population of fast meteors included in the MIF [*Fentzke and Janches*, 2008].

[17] It should be noted that the seasonal variability of MIF used here differs from that derived from observations using meteor radars [*Singer et al.*, 2004]. That study focused on the variability of detected specular underdense meteor trails which are a subset of all meteor detections. Since the main purpose of meteor radar is the measurement of mesospheric winds, only trails for which the wind can be determined are counted, with the result that this can lead to large biases in determining the total meteor flux. In addition, meteor radars cannot measure meteors ablating higher than 100 km, where much of the ablation occurs. These radars also do not see many of the high speed meteor population and so inefficiently measure the apex sources. We conclude that the seasonal variability derived from these measurements is incomplete and subject to bias. This is not the case with the HPLA observations of meteor head-echoes [*Fentzke and Janches*, 2008], where all the events detected are considered in determining the seasonal variation of the MIF.

4. Results and Discussion

[18] The model was run for the period 2004 to 2011, when the GEOS5 analysis data are available. The model outputs for the coordinates of the lidar stations and rocket launching facilities were sampled every 30 min. Otherwise, monthly mean global output was saved. To derive the modeled climatologies of temperature, Fe and other chemical constituents, we use the model output from 2005 to 2011. It should be noted that the Fe lidar observations at the different observatories were made in different periods between 1995 and 2011 (Table 1), and hence at different points in the solar cycle. However, solar cycle effects on the Fe layer appear to be rather small. For example, in the WACCM-Fe run presented in this study, the change in the Fe column abundance from solar minimum (2005 to 2007) to solar maximum (2009 to 2011) ranges from –3% at high SH latitudes to +3% at NH middle to high latitudes. We therefore do not consider solar cycle influences further in this study, although a future paper will examine solar cycle impacts on several of the meteoric metal layers.

4.1. SD-WACCM Model Performance

[19] There have been a number of validation studies of WACCM performance in the MLT region. *Smith* [2012] and *Marsh* [2011] provided detailed overviews of the dynamical processes controlling the MLT and its variability, which also included comparisons of WACCM simulations with observations. Figure 2 compares the July mean climatology of zonal mean temperature and zonal mean zonal wind from the COSPAR International Reference Atmosphere (CIRA) [*Fleming et al.*, 1990] with the SD-WACCM simulations. CIRA and SD-WACCM show similar temperature and wind structures in the MLT region, although there are some significant discrepancies, e.g., SD-WACCM has a mesopause about 2 km lower during polar summer, and has lower altitude for the winter transition from westerly to easterly winds, than CIRA. This is similar to *Smith* [2012], who compared

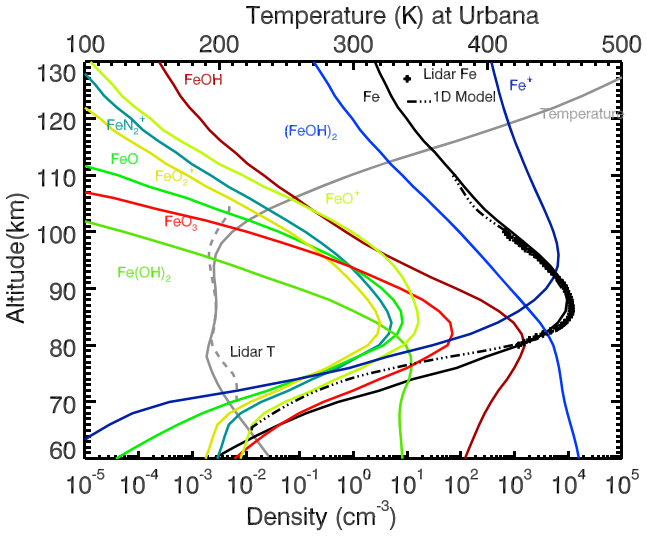

Figure 5. Annual mean profiles of temperature and Fe over Urbana (40°N) from lidar measurements and WACCM-Fe 3-D result, also shown are the simulated Fe from 1-D model and Fe chemical constituents from WACCM-Fe model.

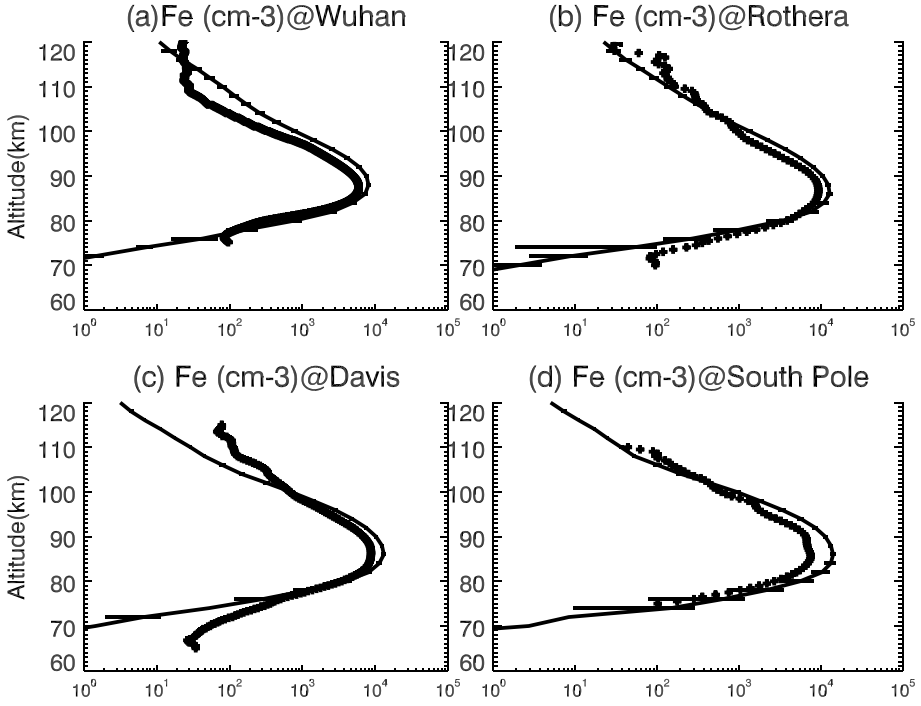

Figure 6. Comparison of lidar observed (symbol) and WACCM-Fe modeled (line) annual mean profiles of Fe concentration (cm^{-3}) for (a) Wuhan, (b) Rothera, (c) Davis, and (d) South Pole stations. The bars indicate the standard deviation of annual mean values from WACCM-Fe during the 7 year run (2005–2011). There is a large degree of variability in the modeled Fe below 80 km where there is a large vertical Fe gradient.

WACCM temperature and zonal mean wind with SABER measurements [*Russell et al.*, 1999] and the UARS Reference Atmosphere Project (URAP) [*Swinbank and Ortland*, 2003] climatology.

[20] Ion chemistry plays an important role in determining the mesospheric Fe layer (the relevant ion-molecule reactions are listed in Table 5), and so we also compare the electron density derived from International Reference Ionosphere (IRI) [*Bilitza*, 2001] with the SD-WACCM simulation. Figure 3 shows the climatological electron density for Rothera. The model captures the seasonal variation of electron density (i.e., maximum electron density in late spring and early summer) and agrees quite well with the IRI electron density below 95 km. However, WACCM significantly underestimates the electron density above 95 km, especially during polar summertime, and so simulations of Fe^+ in this region may have significant errors. This large discrepancy is likely related to electrodynamics, which will be discussed further in section 4.2.

[21] The PMC ice mass and particle effective radius predicted by SD-WACCM can also be compared against measurements. *Hervig et al.* [2009a, 2009b] showed that the PMC ice particles near 69°N are always present from mid-May to end of August 2007. Figure 4 shows the time series of ice mass and effective radius as a function of altitude for 69°N based on 3 day averages, which can be compared directly with SOFIE measurements [*Hervig et al.*, 2009a, 2009b]. The model simulates the timing of the PMC onset and disappearance very well. The PMC size from SOFIE measurements is up to 80 nm, compared with the modeled radius of up to 60 nm. The model has a lower PMC layer and produces too much ice, which is due to the lower and colder mesopause (see temperature comparison in Figure 2).

[22] The main objective of this paper is to develop a global model of meteoric Fe based on our current knowledge on the meteoric input, dynamics, and chemistry. Among the limited number of whole atmosphere models (with interactive chemistry) currently available, SD-WACCM was chosen because it includes most of the important processes required for our purpose. Although the model does exhibit some biases relative to the available mesospheric observations, we show in the following sections that it can produce much of the observed variability in the Fe layer.

4.2. Annual Mean Fe Profiles

[23] Figure 5 shows the annual mean concentration profiles of temperature, Fe, and other iron-bearing chemical species (Fe^+, FeO^+, FeN_2^+, FeO_2^+, FeO, FeO_2, FeO_3, FeOH, $Fe(OH)_2$, $(FeOH)_2$ (i.e., FeOH dimmer)) calculated with WACCM-Fe for Urbana (40°N). Figure 5 also includes the annual mean temperature and Fe profile from lidar measurement as well as the modeled Fe profile from our 1-D model [*Helmer et al.*, 1998]. Here the 1-D model used the seasonally varying Fe MIF (see Figure 1) and required monthly mean variables (temperature, atmospheric density, O_3, O, H, H_2O, K_{zz}, e^-, NO^+, and O_2^+) from WACCM. The observed temperature profile in the MLT is captured satisfactorily by WACCM, although the model has lower temperatures below 80 km and slightly higher temperatures above 90 km.

[24] The observed Fe layer for Urbana peaks around 85 km with an annual mean density of 11,300 cm^{-3}.

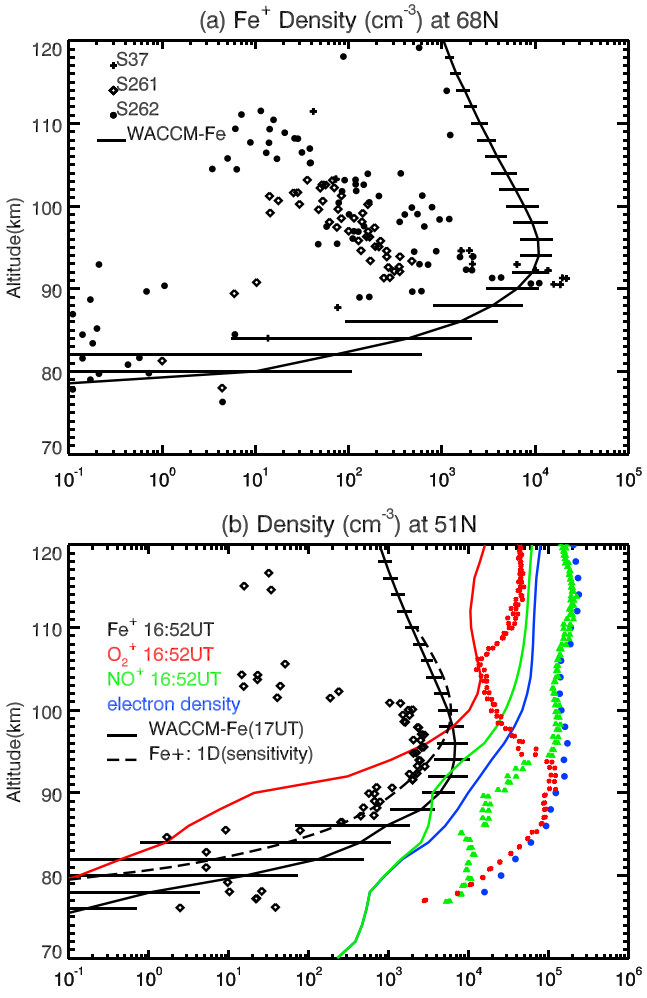

Figure 7. Fe^+ profiles over (a) Kiruna and (b) Red Lake from rocket measurements (symbols) and the model. Also shown are the O_2^+, NO^+, and electron density profiles for Red Lake, and the 1-D model sensitivity result with the rate coefficients for R28a and R28b increased by a factor of 10. The horizontal bars indicate the standard deviation of Fe^+ from WACCM-Fe simulations during the 7 year run (2005–2011).

WACCM-Fe reproduces the observed Fe profile satisfactorily with the Fe MIF shown in Figure 1. The Fe peak density is also at 85 km though it is slightly underestimated (9600 cm^{-3}), while the topside of the Fe layer is slightly overestimated. Fe^+ ions dominate on the topside of the Fe layer above 90 km, because of the conversion of neutral Fe atoms by charge exchange with ambient O_2^+ and NO^+ through reactions R26 and R27 in Table 5 (photoionization reaction J1 in Table 3 is less significant). $(FeOH)_2$, FeOH, and $Fe(OH)_2$ are the dominant reservoirs on the underside of the layer below 85 km. FeO_3 is less significant, and the other Fe-containing molecules are negligible because of their fast reactions with O and H.

[25] Although there is good agreement between model and lidar observation for Urbana (Figure 5), we need to point out that the Fe MIF with an annual mean of 7080 atoms cm^{-2} s^{-1} in Figure 1 is similar to the MIF used by *Gardner et al.* [2011], but is considerably smaller than other estimates [e.g., *Plane et al.*, 2003; *Plane*, 2012]. In earlier 1-D Fe model studies, annual mean Fe MIFs of 38,000 and 34,000 atoms cm^{-2} s^{-1} were used to model the Fe layer at Urbana [*Helmer et al.*, 1998] and South Pole [*Gardner et al.*, 2005], respectively. However, these earlier studies used much larger values of the vertical eddy diffusion coefficient (K_{zz}) in the MLT. *Plane* [2004] showed that the modeled Na total abundance is very sensitive to both MIF and (K_{zz}). We examine this relationship for Fe in section 4.6.

[26] Figure 6 compares the modeled and observed annual mean Fe density for Wuhan, Rothera, Davis, and South Pole. Overall, WACCM-Fe simulates the peak height and width of the Fe layer well. Although the model reproduces the steep bottomside of the Fe layer satisfactorily, except for Davis below 75 km, it significantly overestimates the peak density and topside layer below 100 km for these stations. The observed (modeled) annual mean peak density of Fe is 5940 (8350) cm^{-3} for Wuhan, 9300 (17010) cm^{-3} for Rothera, 8780 (17600) cm^{-3} for Davis, and 7470 (18770) cm^{-3} for South Pole. The possible reasons for this are discussed in section 4.3.

[27] Figure 7 shows measured Fe^+ profiles over Kiruna (68°N, 22°E) during nighttime, and Red Lake (51°N, 267°E) during daytime, compared with the model. Also shown are the O_2^+, NO^+, and electron density profiles for Red Lake. The observed maximum Fe^+ concentration is about 2×10^4 cm^{-3} around 91 km at 68°N and about 2800 cm^{-3} around 93 km during day time at 51°N. WACCM-Fe reproduces satisfactorily both the peak height and concentration of the Fe^+ layer in both cases. However, the model predicts an Fe^+ layer bottomside that is 3 to 5 km too low, and concentrations on the topside above 100 km that are too large by 1 to 2 orders of magnitude. To investigate this, we ran the 1-D model with the rate coefficients for the dissociative electron recombination reactions (R28a and R28b) increased by a factor 10, which is within the likely range for this type of reaction [*Florescu-Mitchell and Mitchell*, 2006]. As shown in Figure 7b, there is now much better agreement on the ion layer bottomside.

[28] Although the ion-neutral collision frequency is still high enough on the topside of the Fe^+ layer below 110 km to allow significant collisional induced ion transport across the magnetic field lines [*Grebowsky and Reese*, 1989], there must also be a significant transport of Fe^+ ions into the thermosphere via the Lorentz $\mathbf{V} \times \mathbf{B}$ force, where $\mathbf{V}$ is the horizontal wind and $\mathbf{B}$ is the Earth's magnetic field [*Carter and Forbes*, 1999]. WACCM does not yet include the Lorentz force, which may explain why the model significantly overpredicts Fe^+ in the lower thermosphere. Further evidence for this is that WACCM reproduces the rocket O_2^+ and NO^+ profiles above 100 km satisfactorily within an order of magnitude (Figure 7b and also electron density comparison for Rothera in Figure 3). These species are much shorter lived (a few hundred seconds, compared with a lifetime for Fe^+ of more than 1 day [*Woodcock et al.*, 2006]), so that vertical transport of O_2^+ and NO^+ is much less important than for the atomic metal ions.

4.3. Latitudinal and Seasonal Variations

[29] Figure 8 shows the monthly mean Fe density from lidar measurements and WACCM-Fe simulations for Urbana and Wuhan. Both stations exhibit a seasonal variation with

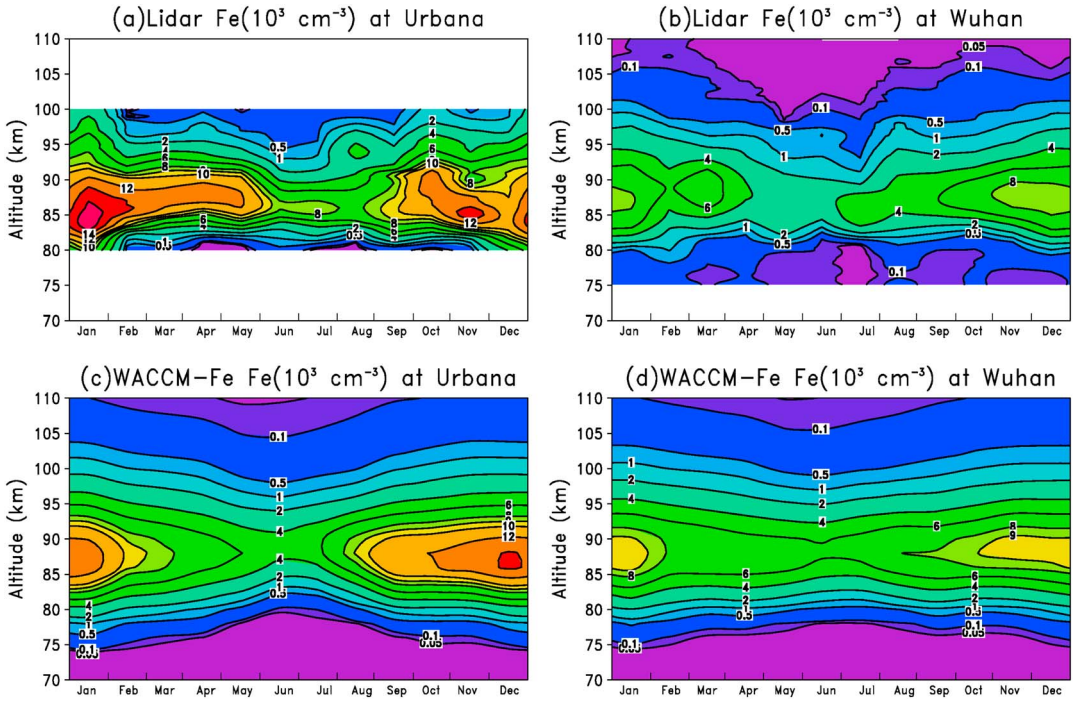

Figure 8. Monthly mean Fe concentration ($\times 10^3$ cm^{-3}) from (a,b) lidar measurements and (c,d) WACCM-Fe simulations (7 years mean from 2005 to 2011) for Urbana and Wuhan.

an early wintertime maximum and summertime minimum Fe density. The summertime (June–August) Fe peak density is about 1.5 to 3 times smaller than in winter. Over Urbana, the peak of the observed Fe layer is at 84–86 km in November–January with the maximum about 16,000 cm^{-3} in January and a second peak density of 14,000 cm^{-3} in November. The Fe peak layer density is smaller and at a slightly higher altitude (about 1 km) over Wuhan. The maximum Fe density for Wuhan is about 8000 cm^{-3} observed between November and January. WACCM-Fe simulates the observed seasonal Fe variation quite well for both stations. The model also captures the observed wintertime Fe peak layer and maximum density with about 14,000 cm^{-3} for Urbana and about 9000 cm^{-3} for Wuhan. In summer, the model slightly underestimates the Fe density at Urbana but overestimates at Wuhan. Overall, the model simulates the observed Fe layer at Urbana and Wuhan in the NH midlatitudes quite well.

[30] Figure 9 is analogous to Figure 8, comparing the model with observations at the high-latitude SH stations of Rothera, Davis, and South Pole. The observed Fe density over Davis is determined every 2 min with an altitude resolution of 200 m. At this resolution the detection limit for Fe in the most challenging observing conditions (highest solar elevation in the middle of summer) is around 250 cm^{-3}. After first averaging the densities of each day, the seasonal densities are then obtained by a 14 day Hanning filter. The Hanning filter was chosen since a harmonic fit with annual and semiannual component cannot reproduce the observed density minimum in December because of its short duration of only a few weeks. The small-scale structures for Davis in Figure 9 were caused by strong variations in the Fe density at all scales, including sporadic layers which are not rejected here. As shown by *Lübken et al.* [2011], tides have a strong influence on the Fe layer. The influence of tides is largely removed here by taking daily means and by averaging over approximately 2000 h of observations that cover all local times. The observed Fe layers at these SH locations have fairly similar seasonal variations and slightly lower peak heights (84–85 km) than at NH midlatitudes. The maximum Fe density of 16,000 cm^{-3} is observed in April for Rothera and July for Davis. Lidar observations show a smaller maximum Fe concentration (12,000 cm^{-3}) at South Pole. An interesting feature is that the summer Fe peak height is about 5 km higher than in winter at these SH high-latitude locations. This is due to the substantial depletion of Fe at PMC altitudes during the polar summer [*Plane et al.*, 2004]. WACCM-Fe simulates the seasonal variation in the Fe peak height reasonably well. Note that these measurements are taken in different years (Table 1) and there is year-to-year variability of the Fe layer. However, the model significantly overestimates the winter Fe density and underestimates the summer Fe concentration for SH high latitudes (the reason for this is discussed below).

[31] Figure 10 compares the monthly mean total column Fe abundance measured at the five lidar stations with WACCM-Fe simulations. Both the lidar measurements and the model exhibit seasonal variations of total column abundance with a winter maximum and a summer minimum. Similar to the results shown in the seasonal Fe concentration comparison as a function of altitude in Figures 8 and 9, here again the model simulates the observations at Urbana well, but overestimates the wintertime Fe for the other stations especially for SH high latitudes, which is partly due to the large differences between the modeled and observed temperatures during polar winter in the upper mesosphere (Figure 11).

[32] The annual mean column Fe abundances measured by lidar and predicted by WACCM-Fe are summarized in

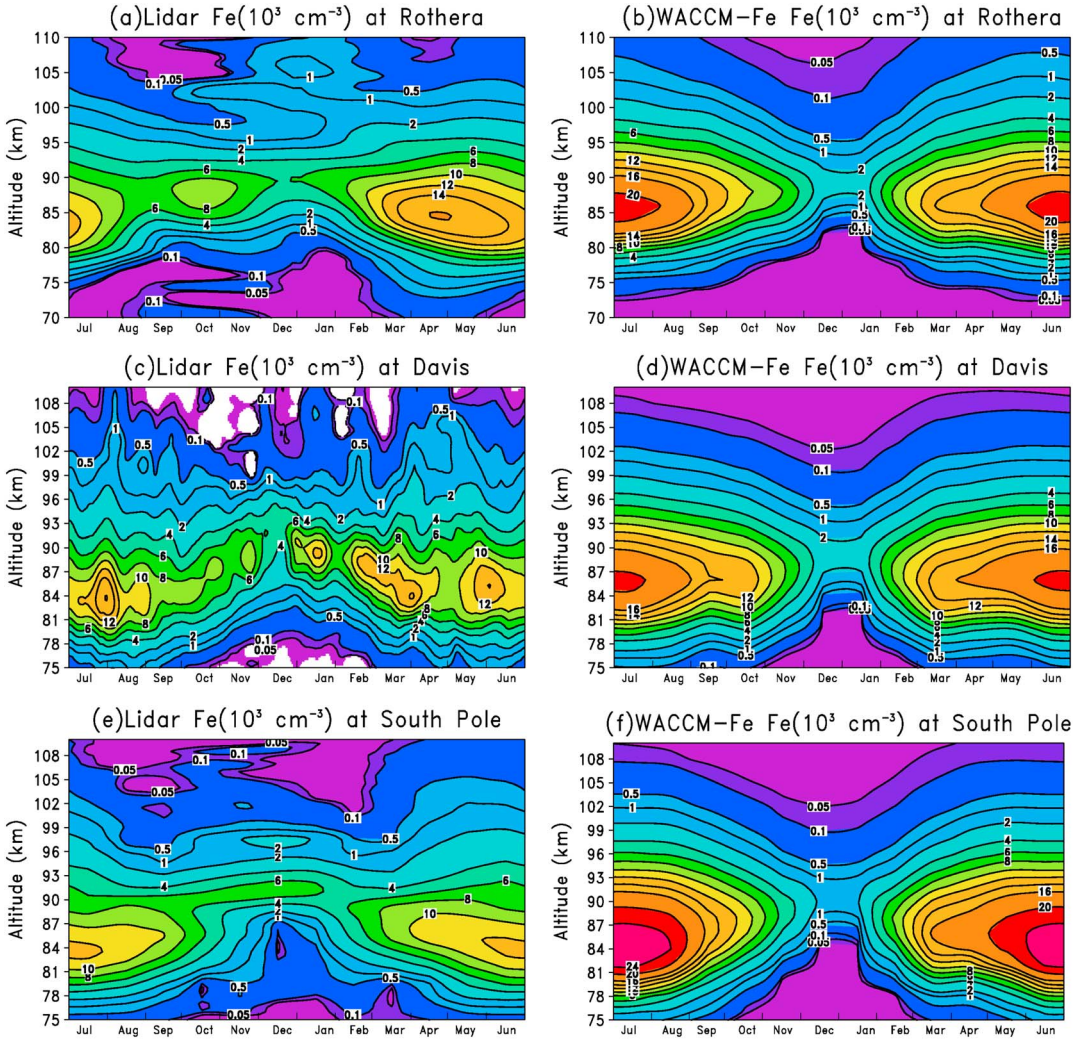

Figure 9. As in Figure 8, but for (a,b) Rothera, (c,d) Davis, and (e,f) South Pole.

Table 6. The measured mean of 11.5×10^9 cm^{-2} for Urbana agrees well with the WACCM-Fe mean of 11.1×10^9 cm^{-2} (the annual means of individual years in the 7 year period range from 9.9 to 12.9×10^9 cm^{-2}). The lower column abundance (7.5×10^9 cm^{-2}) at Wuhan is also satisfactorily captured by the model (9.5×10^9 cm^{-2}, ranging from 8.0 to 11.3×10^9 cm^{-2} in individual years). In contrast, Table 6 shows that the model overestimates the SH high-latitude annual mean total column Fe abundance by about 40% at Rothera and Davis and 80% at South Pole. Since several of the neutral reactions in Table 4 are significantly temperature-dependent (e.g., R7, R11, R12), it is useful to explore the correlation between temperature and Fe density, and to see if this is a cause of the model-observation discrepancy.

[33] Figure 11 shows the monthly mean temperature profiles from lidar measurements [*Pan and Gardner*, 2003] and the WACCM-Fe simulation for South Pole (the extreme case) as well as the temperature difference between the model and observations. The correlation between Fe density and temperature is also shown in Figure 11d. The observed mean mesopause (i.e., the altitude of minimum temperature in the MLT) during November–February over South Pole is located at around 85–90 km with a mean temperature as low as 140 K in December (lidar observations are not useful for measuring temperature when the mesopause is very cold and there is a low density of metal atoms). The temperature during the winter period is warmer (180 K) and the mesopause is higher (around 100 km). It is well-known that this is caused by the large-scale meridional circulation with upwelling air masses over the summer pole which flow toward the winter pole and then downward in the winter polar vortex [*Brasseur and Solomon*, 2005]. WACCM-Fe captures the changing mesopause height very well, but exhibits a colder summer mesopause (130 K) and a warmer winter mesopause (200 K). This indicates that there is a stronger meridional circulation in WACCM than is observed at South Pole. Figure 11d shows that there is a strong positive correlation between Fe density and temperature around the peak of the Fe layer (the correlation coefficient is close to 1.0 at ∼88 km), which indicates there will be more Fe if the temperature is higher. In contrast, on the topside of the Fe layer above 90 km, the correlation between Fe and temperature decreases rapidly, and there is a significant anticorrelation (∼ –0.8) around 100 km. Both

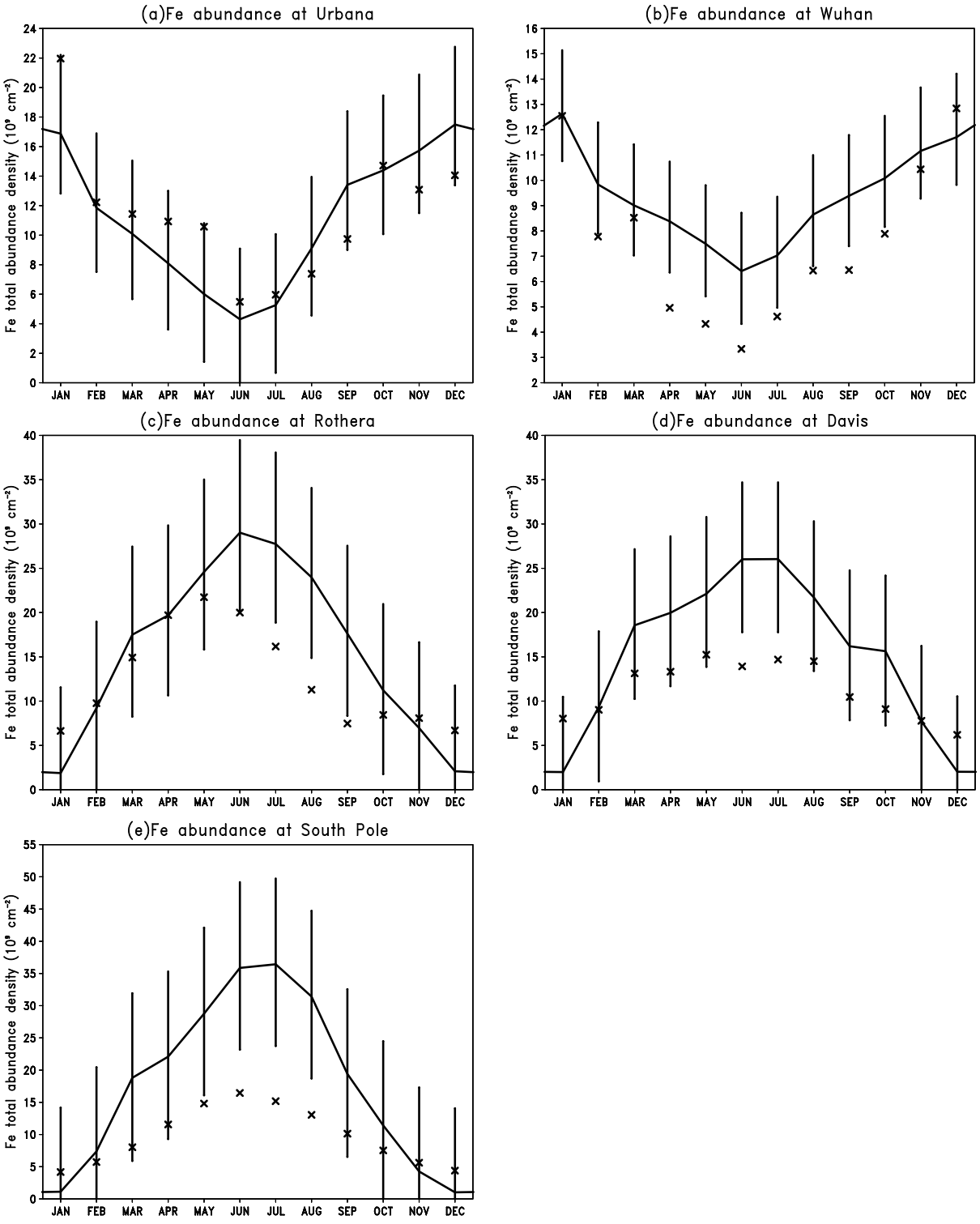

Figure 10. Monthly mean total column abundance of Fe from lidar measurements (symbols) and WACCM-Fe simulations (solid line, 7 year mean from 2005 to 2011) for (a) Urbana, (b) Wuhan, (c) Rothera, (d) Davis, and (e) South Pole. The bars indicate the standard deviation of annual monthly mean values from WACCM-Fe during the 7 year run (2005–2011).

these features are well captured by the model (Figure 8c). The study by *Gardner et al.* [2011] proposed that the convergence of the meridional flux of Fe over the South Pole plays a crucial role in maintaining the high abundance of the wintertime Fe and Na layers observed at this site. Therefore, the overestimated winter Fe density for South Pole predicted by WACCM (Figures 9 and 10) is consistent with the meridional circulation being too strong in the model, causing too large a convergence of Fe species over the pole and overpredicting the temperature between 75 and

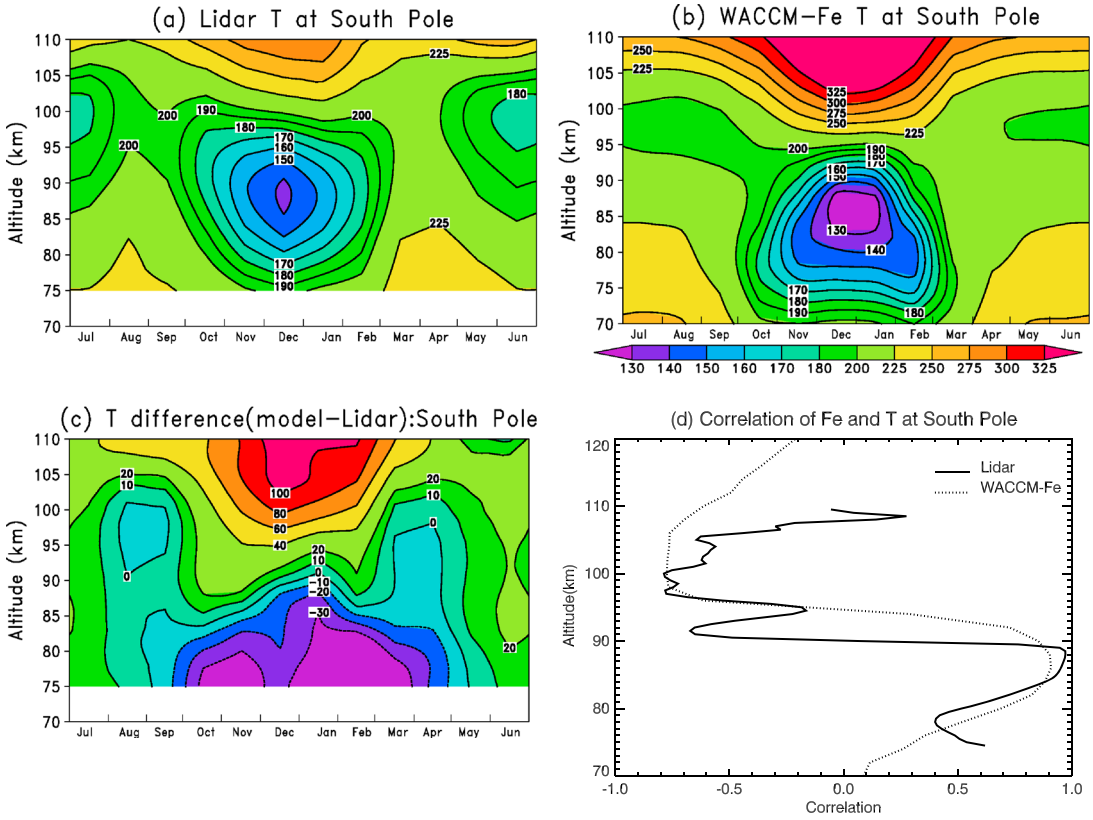

Figure 11. Monthly mean temperatures from (a) lidar measurements and (b) WACCM-Fe simulations for South Pole as well as the (c) temperature difference between the model and observations. Also shown is (d) the correlation between annual mean Fe density and temperature from observations and the model as a function of height.

90 km. The model underestimates the observed summer Fe density for South Pole because WACCM has a colder mesosphere and mesopause (temperature difference is up to 30 K below 90 km) and warmer lower thermosphere (temperature difference is more than 80 K above 100 km) in summer (Figure 11c). Again, the lower modeled temperature below 90 km decreases Fe because the Fe reservoirs are more stable against reaction with H atoms. The significant activation energies of R10–R12 (Table 4) lead to a positive correlation between temperature and Fe below 90 km (Figure 11d).

4.4. Tidal Influences on the Fe Layer

[34] Atmospheric tides are one of the more dominant dynamical processes in the MLT [*Forbes et al.*, 2007]. Metal layers, with their relatively long chemical lifetimes, are ideal tracers for atmospheric dynamical process, including tides (Marsh et al., submitted manuscript, 2013). Recently, *Lübken et al.* [2011] found from lidar measurements that tides have a strong influence on the Fe layer. Figure 12 shows 3 days of modeled temperature and Fe mixing ratio sampled every 30 min for the location of Urbana from 1 July 2005, as well as their perturbations (difference from the 3 day average at each height). During this summer period, the mesopause occurs around 80 km and high Fe volume mixing ratios are predicted between 90 and 95 km, with a maximum 200 pptv (the peak atomic Fe density is around 90 km with a maximum value of 5000 cm^{-3}, not shown in the figure). One striking feature is the strong diurnal variation on the underside of the Fe layer below 78 km. In the model, this is caused by the solar-driven diurnal variation in atomic H and O, particularly through the reaction of H with the main reservoir species FeOH (reaction R12 in Table 4). This diurnal variation in atomic Fe has recently been observed by *Yu et al.* [2012]. The photolysis of FeOH (J1 in Table 3) may also play a role, but the photolysis cross section of this molecule has not yet been measured. Above 100 km the model predicts a semidiurnal variation in temperature associated with the semidiurnal tide. The change in Fe at these heights is diurnal with a maximum at noon, rather than semidiurnal, and so appears to be largely responding to photochemical rather than tidal forcing. However, at and

Table 6. Annual Mean Fe Total Column Abundance ($\times 10^9$ cm^{-2})

	Urbana	Wuhan	Rothera	Davis	South Pole
Lidar	11.5	7.5	12.3	11.3	9.7
WACCM-Fe	11.1	9.5	16.3	15.7	18.3
WACCM(min–max)	(9.9–12.9)	(8.0–11.3)	(14.2–18.8)	(13.2–18.8)	(14.9–22.3)

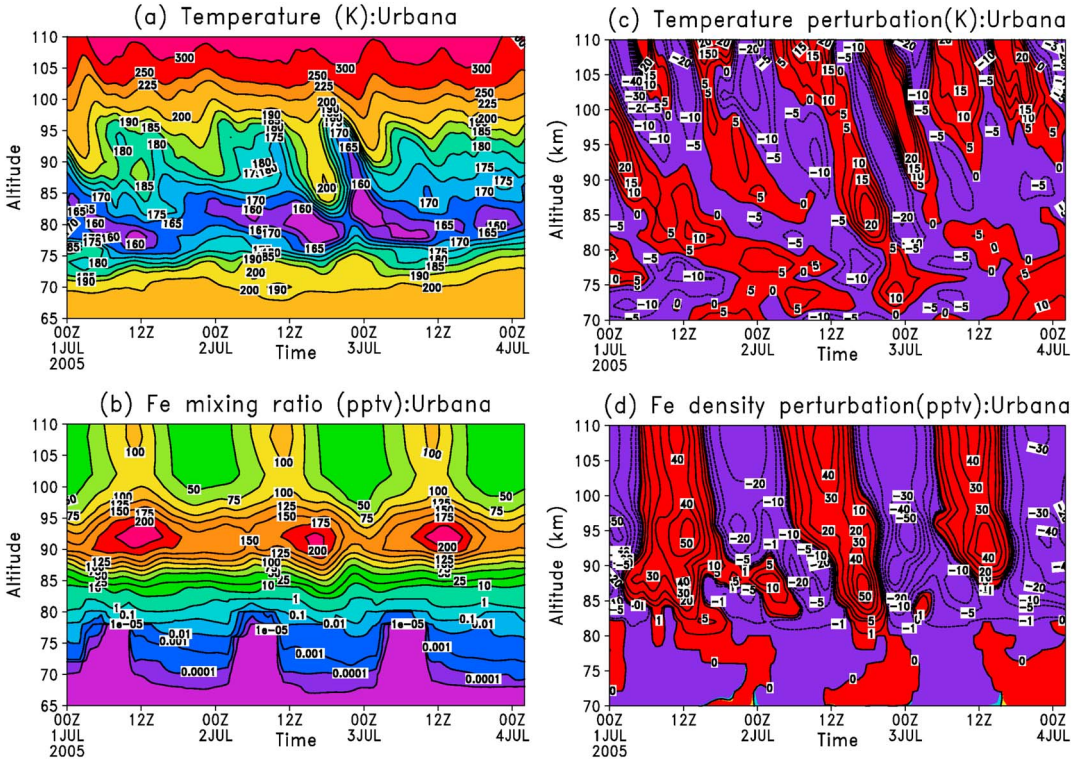

Figure 12. Three days of model output sampled every 30 min for Urbana from 1 July 2005: (a) temperature (K); (b) Fe mixing ratio (pptv); (c) perturbation in temperature (difference from the 3 day average); (d) perturbation in Fe mixing ratio. The time in the plot is Universal Time (UT). Local time = UT – 6.

below the peak of the layer, the Fe variations closely correlate with the tidally driven temperature fluctuations (see also Figure 11). There is a positive correlation with temperature below the Fe peak, and both have a diurnal variation. Since the Fe concentration increases with height below the peak, a downward tidal motion associated with the diurnal tide would lead to an increase in Fe at a particular height. The vertical motion would also cause an increase in temperature via adiabatic warming. Both Fe and temperature would increase during the entire downward phase of the tide (peaking at the point the wind is zero), at which point upward motion would then lead to an Fe decrease and adiabatic cooling. Recently, *Sakazaki et al.* [2012] showed that diurnal tidal amplitudes in meteorological analyses (although they did not include the GEOS5 meteorological data set used here) tend to be underestimated by 30–50% in the upper stratosphere and lower mesosphere. In a future study we will investigate the impacts of using different meteorological analyses on the modeled Fe layer.

4.5. Column Abundances, Centroid Heights and RMS Widths of the Fe and Fe^+ Layers

[35] Figure 13 shows the modeled zonal mean monthly mean Fe and Fe^+ column abundances integrated from 70 to 120 km. Fe^+ at middle to high latitudes (30°-60°) peaks in August for the NH and in February for the SH, whereas Fe has a winter maximum abundance. In the tropics, Fe^+ is relatively constant with maximum concentrations during equinox. Figure 14 shows the ratio of Fe^+ to Fe from Figure 13. The ratio ranges from 0.3 to 6; there is a clear seasonal variation with a maximum ratio in summer and minimum in winter at high latitudes, which tracks the daily integrated photoionization rates. The global annual mean of the Fe^+:Fe ratio is about 1.0, which is similar to the modeled Na^+:Na ratio (Marsh et al., submitted manuscript, 2013). The abundance ratio of modeled Fe^+ to Fe appears to be overestimated, the ratio of observed Fe^+ (obtained from a limited set of rocket-borne mass spectrometric data) to the observed neutral Fe (from lidar measurement) is about 0.2 [*Murad and Williams*, 2002]. However, this is most likely mainly due to the model overestimating Fe^+ above 95 km (Figure 7).

[36] In addition to the Fe column abundance in Figure 13, the centroid height and RMS layer width are two important parameters for characterizing the seasonal variations in dynamical and chemical effects on the layer [*Gardner et al.*, 1986]. The monthly mean centroid height and RMS layer width, calculated from the monthly mean Fe density profiles, are shown in Figure 15. This shows that the centroid height of Fe has a semiannual variation with highest altitude in late June for the NH high latitudes, December–January for SH high latitudes and late January for tropical regions. The RMS layer width has a strong annual variation with a maximum in winter and minimum in summer, similar to the Fe column abundance in Figure 13.

4.6. Sensitivity Tests

[37] The previous sections show that the general performance of WACCM-Fe model is satisfactory, although there are some areas of discrepancy. One important question is that whether the seasonally varying MIF used in the model plays an important role in determining the modeled seasonal variability of the Fe layer. We therefore also ran the model using

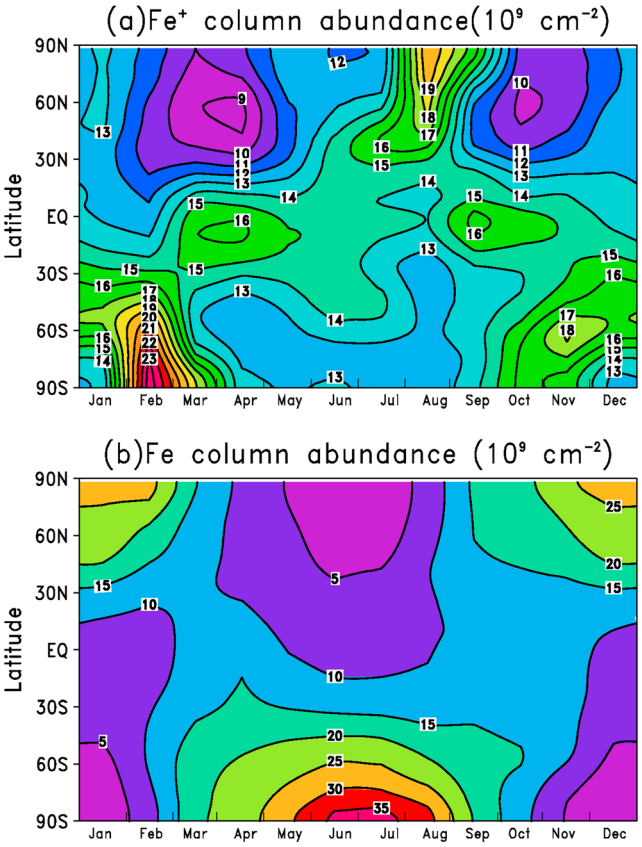

Figure 13. Mean (a) Fe^+ and (b) Fe column abundances ($\times 10^9$ cm^{-2}) between 70 and 120 km.

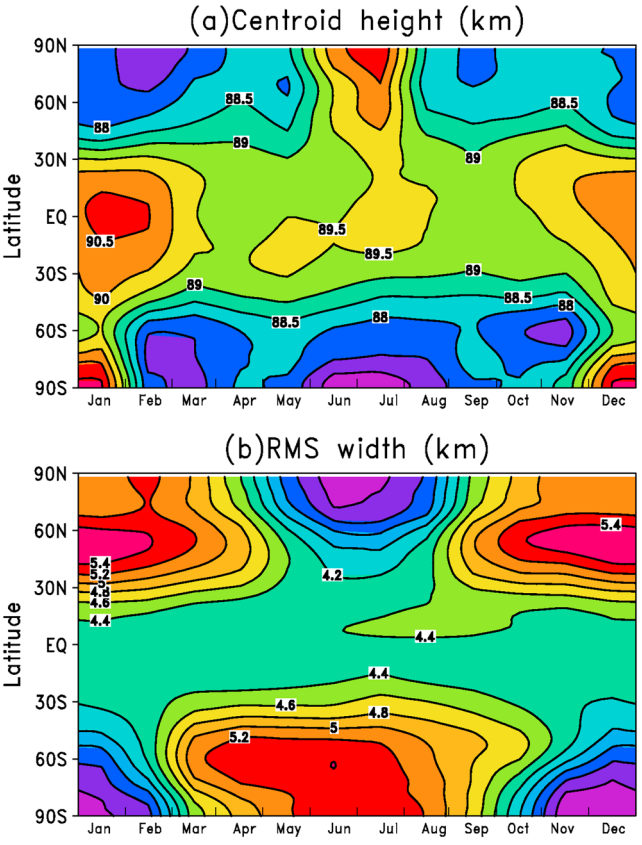

Figure 15. Mean (a) centroid height (km) and (b) RMS width (km) of the Fe layer as a function of latitude and month calculated from 2005 to 2011 using WACCM-Fe.

a constant MIF to investigate the sensitivity of the seasonal Fe layer to the MIF. Figure 16a shows the relative Fe MIF difference (%) between the seasonal varying MIF and constant (global annual mean) MIF, which ranges from –35% in early spring to +20% in early autumn. Figure 16b shows the resulting relative difference (%) of the modeled Fe column abundance between the seasonally varying and constant MIF. Inspection of the two parts of the figure shows that the relative difference in the Fe column abundance in the NH correlates well with the relative difference between the seasonal and constant MIF. In contrast, the expected decrease in the relative Fe column abundance does not occur in the SH spring (September–October) at high latitudes, when the seasonal MIF is at a minimum. This striking difference with the NH is most likely due to the much stronger southward mesospheric mean meridional circulation during July and August driven by the small-scale gravity wave-induced momentum flux divergence. This circulation transports Fe from the northern hemisphere (where the MIF is increasing in early NH autumn (Figure 1)), compensating for the decreasing MIF in the SH spring.

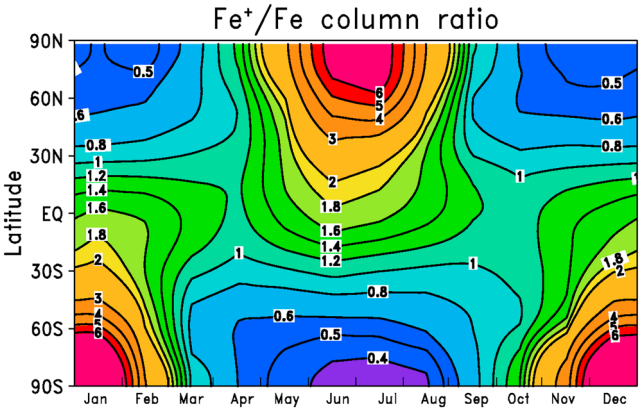

Figure 14. Mean ratio of the column abundances of Fe^+ and Fe as a function of latitude and month calculated from 2005 to 2011 using WACCM-Fe.

[38] To explore the sensitivity to the rate coefficients in the model, for computational efficiency, we used the 1-D instead of the full 3-D model. This exercise is important because while the majority of the rate coefficients in Tables 4 and 5 have been measured in the laboratory, a few have been fitted by optimizing models to give good agreement with lidar observations [*Helmer et al.*, 1998; *Plane et al.*, 1999]. Figure 17 shows the sensitivity of the total column abundance of Fe to a selection of the rate coefficients in Tables 4 and 5. The relative change in the Fe column abundance is shown when each rate coefficient is changed by ±20%, the choice of percentage is somewhat arbitrary, but 20% is a typical upper limit to the uncertainty of a rate coefficient for a metallic species measured in the laboratory under mesospheric conditions [*Plane*, 2002].

[39] The greatest model sensitivity is to the rate coefficients for the dissociative recombination reactions R28a and

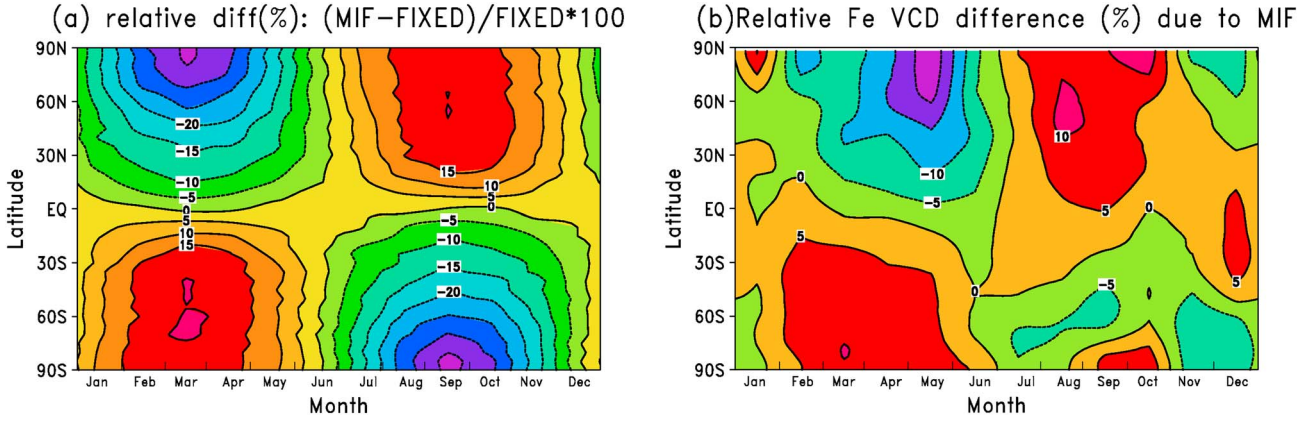

Figure 16. (a) Relative difference (%) between the seasonal varying MIF and constant (global annual mean) MIF, (b) Relative difference (%) between the modeled Fe column abundance for the seasonal and constant MIF.

R28b ($FeO^+ + e^-$, $FeO_2^+ + e^-$). In the current model, these rate coefficients are set equal to typical values for this type of process [*Florescu-Mitchell and Mitchell*, 2006]. Clearly, the rate coefficients for these reactions need to be measured in the future. The model is also particularly sensitive to R21 ($FeO^+ + O$), which competes with R28a to prevent neutralization of FeO^+ after it forms from $Fe^+ + O_3$ (R20). However, the rate coefficients for R20 and R21 have been measured (Table 5).

[40] For the Fe neutral chemistry, the most sensitive reactions are R1 ($Fe + O_3$), R2 ($FeO + O$), R4 ($FeO + O_2$), and R12 ($FeOH + H$). The first three reactions have been studied under mesospheric conditions (Table 4). Although the rate coefficient for R12 has been estimated indirectly [*Self and Plane*, 2003], this quantity should be measured once a method for the direct detection of FeOH becomes available, which would also permit a study of the possible reaction of FeOH with O_3 to form OFeOH (a single molecule of the stable mineral goethite which could be a precursor of meteoric smoke).

[41] In the last part of this section, we examine the sensitivity of the Fe column abundance to the rate of vertical transport, parameterized in the 1-D model by the eddy diffusion coefficient K_{zz}. Figure 18 shows the annual mean column abundance of Fe as a function of the meteoric input and averaged K_{zz} between 80 and 90 km (calculated using the 1-D model for 40°N). The MIF here is converted into the global daily input of cosmic dust, for ease of comparison with other estimates of this quantity [*Plane*, 2012]. The annual mean MIF of Fe used in WACCM-Fe corresponds to 2.1 t d^{-1}, and the mean value of K_{zz} in WACCM between 80 and 90 km at 40°N is 5 m^2 s^{-1}. This combination reproduces the observed Fe column abundance at Urbana of 11 × 10^9 cm^{-2}. This figure also implies that to sustain the same total column abundance of Fe, the model requires a higher value for the MIF when faster vertical diffusion (and subsequent faster removal of meteoritic material from the atmosphere) is implemented in the model via higher K_{zz}. The reverse also holds, i.e., a lower MIF can maintain the same Fe abundance if a lower K_{zz} is used. Note that an input rate of 2.1 t d^{-1} is at the low end of the estimates of the daily input of cosmic dust input which range up to nearly 300 t d^{-1} [*Plane*, 2012]. Inspection of Figure 18 shows that in order to sustain a meteoric input of more than 20 t d^{-1}, K_{zz} between 80 and 90 km would need to be greater than 200 m^2 s^{-1}. This seems unlikely, although recently *Grygalashvyly et al.* [2012] estimated the vertical diffusion coefficient from the simulated distributions of different long-lived chemical constituents using a gravity-wave resolving GCM. They showed that the diffusion coefficient is clearly dominated by mesoscale gravity waves, which can generate K_{zz} values larger than 250 m^2 s^{-1} at 88 km during polar winter.

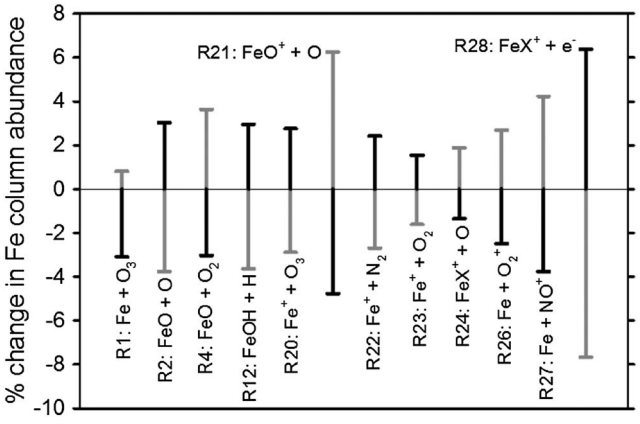

Figure 17. Percent change in the Fe column abundance (calculated with the 1-D model for 40°N) to a 20% increase (black bar) or a 20% decrease (grey bar) in selected rate coefficients from Tables 4 and 5.

[42] If the input really is an order of magnitude larger than required in WACCM-Fe, this may indicate that Fe compounds are transported more rapidly downward in the MLT than just by eddy diffusion and the residual circulation. For example, *Gardner and Liu* [2010] have proposed that dynamical transport caused by dissipating gravity waves, and chemical transport involving wave action and irreversible chemical loss at a lower altitude (e.g., to form meteor smoke), can produce a substantial downward net flux of constituents in the MLT.

[43] To further investigate the impact of gravity wave breaking on vertical eddy diffusion and the modeled Fe layer, we also ran a 2 year (2004–2005) SD-WACCM sensi-

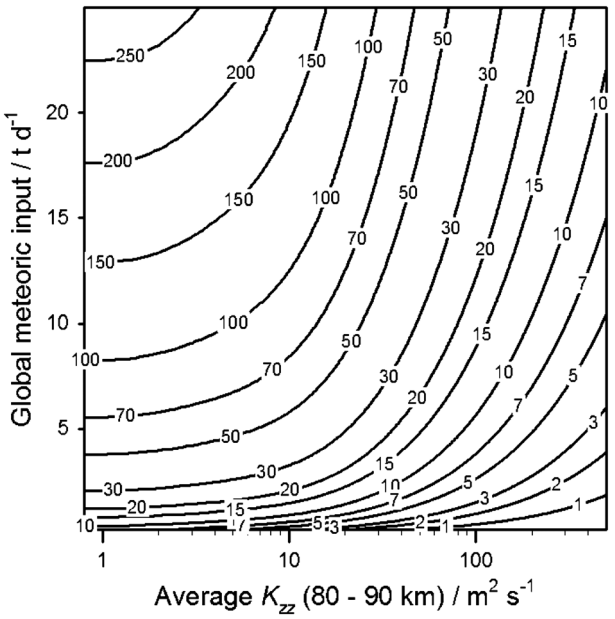

Figure 18. The Fe column abundance ($\times 10^9$ cm^{-2}, calculated from the 1-D model for 40°N) to the global meteoric input rate and K_{zz} averaged between 80 and 90 km.

tivity experiment by adjusting a key variable in the gravity wave parameterization: the equivalent Prandtl number (Pr), which is the ratio of momentum flux to heat flux. Pr is used in the calculation of K_{zz} as described in *Garcia et al.* [2007] and *Smith* [2012]. K_{zz} scales with the inverse of Pr, so decreasing Pr will increase the eddy diffusion. *Liu* [2009] estimated the eddy momentum and thermal diffusion coefficients from measured gravity wave momentum and heat fluxes using lidar observations, from which he found that the annual mean Pr profile can be in the range of 1–4 in the MLT. *Fritts and Alexander* [2003] reported that the Pr value associated with gravity wave breaking is poorly defined at present and may vary with height in the range of 3–10. The standard WACCM model uses a value of Pr equal to 4. Figure 19a shows the zonal mean annual mean of K_{zz} as a function of latitude from 70 to 110 km from the standard model run for 2005. K_{zz} gradually increases with height and has larger values around 60° and a second maximum in the tropics in the lower thermosphere above the mesopause. These are the regions where vertically propagating waves begin to break when the temperature lapse rate exhibits an abrupt change [*Whiteway and Carswell*, 1995]. The distribution of the K_{zz} in the MLT from the standard model is similar to the WACCM multiyear climatology shown by *Smith* [2012]. The maximum K_{zz} values in the standard model between 85 and 100 km are in the range of 5–30 m^2 s^{-1} are much smaller than the eddy diffusion estimated by *Liu* [2009] (100–500 m^2 s^{-1}). Note, however, this is an annual mean, and individual values can be substantially larger for short periods (<1 day). In the tropical region, the annual mean value of K_{zz} from 70 to 80 km is about 0.5–2 m^2 s^{-1}, which is comparable with values in the range (1–5) m^2 s^{-1} determined from long-term VHF radar observations at Gadanki (13.5°N) [*Rao et al.*, 2001].

[44] As a sensitivity test, we performed an identical 2 year simulation where Pr was set equal to 2. Figure 19b shows

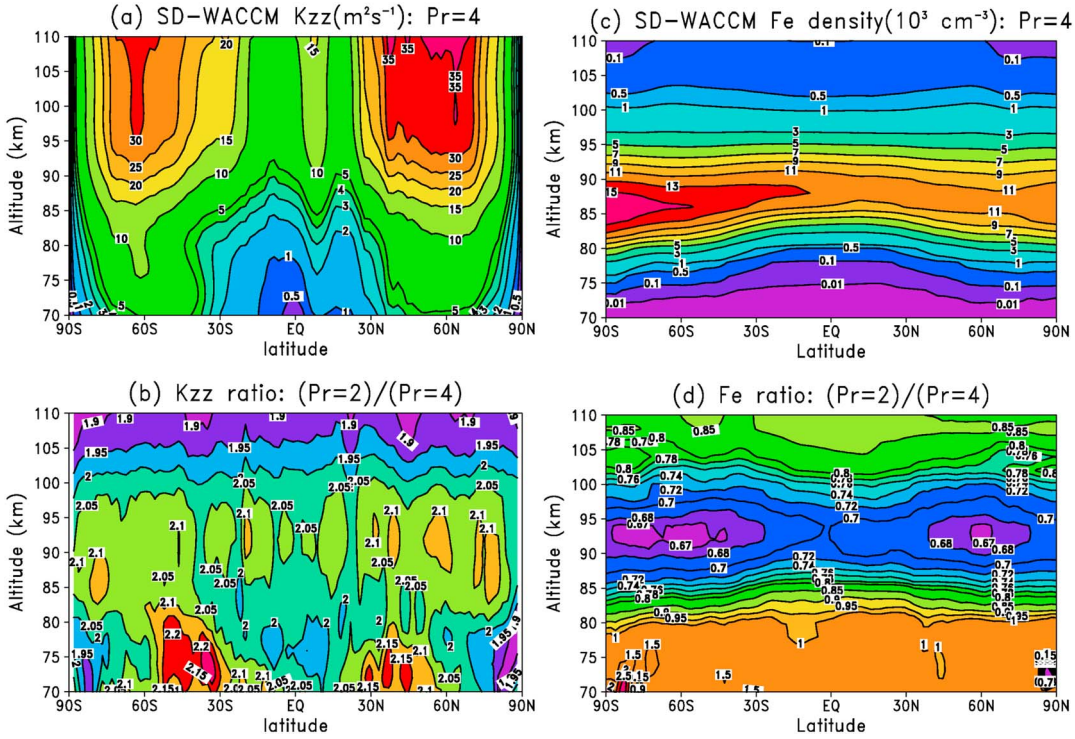

Figure 19. Zonally averaged annual mean profiles as a function of latitude from 70 to 110 km of: (a) modeled K_{zz} from the standard model run (Pr = 4) for 2005; (b) the ratio of K_{zz} between the sensitivity run (Pr = 2) and the standard model; (c) the Fe density from the standard model run; (d) the ratio of Fe density between the sensitivity run (Pr = 2) and the standard model.

the ratio of K_{zz} between the sensitivity (Pr = 2) and the standard (Pr = 4) simulations. As expected, decreasing Pr in the model by a factor of 2 increases the modeled K_{zz} around the same factor in the MLT (Figure 19b). Figures 19c and19d show the corresponding modeled Fe density and the resulting ratio. Halving Pr in the model causes a significant decrease in the Fe density between 85 and 100 km (20–33%), and an increase by over 50% below 80 km. These results are in sensible accord with the 1-D model results in Figure 18. It should be noted that the modeled temperature and Fe distributions are broadly similar for the Pr = 4 and Pr = 2 runs. The model has a colder mesopause (temperature decreases by about 10 K around 90 km in the polar summer and 14 K around 100 km in the polar winter) when Pr value in WACCM is decreased from 4 to 2 (not shown). The modeled winter Fe peak density then decreases from 24,000 cm^{-3} to 16,000 cm^{-3}, which is still slightly higher than the observed 12,000 cm^{-3} for South Pole (not shown).

5. Summary

[45] In this paper we have described the first global atmospheric model of meteoric iron (WACCM-Fe), which is constructed with three components: a whole atmosphere community climate model (WACCM); neutral and ion-molecule iron chemistry in the MLT; and the MIF describing the injection of meteoric Fe into the atmosphere. WACCM-Fe has been used to perform an 8 year simulation over the period 2004–2011. In this simulation WACCM was nudged below 60 km using temperature, specific humidity and horizontal winds from GEOS5 meteorological reanalyses over the same period. The model has been evaluated using lidar Fe measurements from a number of locations, as well as a limited set of rocket-borne mass spectrometric measurements of Fe^+. We have mainly focused on the performance of WACCM-Fe for modeling the climatological behavior of the neutral Fe layer. The model satisfactorily predicts the seasonal variation of the Fe layer at the midlatitude NH stations of Urbana and Wuhan (i.e., characteristic features such as the peak density, peak height, topside and bottomside layer scale heights, and the total column abundance). However, the model overestimates the wintertime Fe abundance for three SH high-latitude stations, which is mainly due to the warmer temperatures and greater convergence over the pole predicted by the model. The model also overestimates the peak Fe^+ concentration in the lower thermosphere, which appears to arise because WACCM does not include the Lorentz force which transports long-lived metallic ions further up into the thermosphere.

[46] Most global general circulation models describe the vertical transport of minor constituents in the MLT by K_{zz}, which is treated analogously to molecular diffusion and operates on mixing ratio gradients. Eddy diffusion in the MLT is largely generated by breaking gravity waves which propagate up from the lower atmosphere. Sensitivity studies using the same chemistry in a 1-D model highlights that the modeled total Fe abundance is very sensitive to K_{zz} and the meteor input rate. The small global input rate of only about 2 t d^{-1} required for WACCM-Fe may imply that the role of dissipating gravity waves in the vertical transport of minor constituents in the MLT needs to be considered.

[47] **Acknowledgments.** This work was supported by the UK Natural Environment Research Council (NERC grant NE/G019487/1). The MIF was developed under NSF grants ATM-05311464, ATM-0525655, ATM-0634650, and AST-0908118 to NorthWest Research Associates. The Fe lidar data for Urbana, Rothera, and South Pole were provided by C. S. Gardner (University of Illinois at Urbana-Champaign). We also thank R. J. Morris from Australian Antarctic Division for supporting the lidar observations at Davis. CIRA data is obtained via the British Atmospheric Data Centre. The authors also acknowledge three anonymous reviewers for their useful comments.

References

Alpers, M., J. Höffner, and U. von Zahn (1990), Iron atom densities in the polar mesosphere from lidar observations, *Geophys. Res. Lett.*, *17*, 2345–2348, doi:10.1029/GL017i013p02345.

Alpers, M., J. Höffner, and U. von Zahn (1994), Sporadic Fe and E layers at polar, middle, and low latitudes, *J. Geophys. Res.*, *99*(A8), 14,971–14,985, doi:10.1029/94JA00589.

Bautista, M. A., P. Romano, and A. K. Pradhan (1998), Resonance-averaged photoionization cross sections for astrophysical models, *Astrophys. J. Suppl. Ser.*, *118*, 259–265, doi:10.1086/313132.

Bilitza, D. (2001), International Reference Ionosphere 2000, *Radio Sci.*, *36*(2), 261–275.

Brasseur, G. P., and S. Solomon (2005), *Aeronomy of the Middle Atmosphere: Chemistry and Physics of the Stratosphere and Mesosphere*, 644 pp., Springer, Berlin.

Carter, L. N., and J. M. Forbes (1999), Global transport and localized layering of metallic ions in the upper atmosphere, *Ann. Geophys.*, *17*, 190–209.

Ceplecha, Z., J. Borovička, W. G. Elford, D. O. ReVelle, R. L. Hawkes, V. Porubčan, and M. Šimek (1998), Meteor phenomena and bodies, *Space Sci. Rev.*, *85*, 327–471.

Chen, L., and F. Yi (2011), Average properties and small-scale variations of the mesospheric Na and Fe layers as observed simultaneously by two closely colocated lidars at 30° N, *Ann. Geophys.*, *29*, 1037–1048, doi:10.5194/angeo-29-1037-2011.

Chu, X., Z. Yu, C. S. Gardner, C. Chen, and W. Fong (2011a), Lidar observations of neutral Fe layers and fast gravity waves in the thermosphere (110–155 km) at McMurdo (77.8°S, 166.7°E), Antarctica, *Geophys. Res. Lett.*, *38*, L23807, doi:10.1029/2011GL050016.

Chu, X., W. Huang, W. Fong, Z. Yu, Z. Wang, J. A. Smith, and C. S. Gardner (2011b), First lidar observations of polar mesospheric clouds and Fe temperatures at McMurdo (77.8°S, 166.7°E), Antarctica, *Geophys. Res. Lett.*, *38*, L16810, doi:10.1029/2011GL048373.

Fan, Z. Y., J. M. C. Plane, J. Gumbel, J. Stegman, and E. J. Llewellyn (2007), Satellite measurements of the global mesospheric sodium layer, *Atmos. Chem. Phys.*, *7*, 4107–4115, doi:10.5194/acp-7-4107-2007.

Fentzke, J. T., and D. Janches (2008), A semi-empirical model of the contribution from sporadic meteoroid sources on the meteor input function in the MLT observed at Arecibo, *J. Geophys. Res.*, *113*, A03304, doi:10.1029/2007JA012531.

Frisch, M. J., et al. (2009), *Gaussian 09, Revision A.1.*, Gaussian, Inc., Wallingford, Conn.

Fleming, E. L., S. Chandra, J. J. Barnett, and M. Corney (1990), Zonal mean temperature, pressure, zonal wind and geopotential height as functions of latitude, *Adv. Space Res.*, *10*, 11–59.

Florescu-Mitchell, A. I., and J. B. A. Mitchell (2006), Dissociative recombination, *Phys. Rep.*, *430*, 277–374, doi:10.1016/j.physrep.2006.04.002.

Forbes, J. M., M. E. Hagan, and X. Zhang (2007), Seasonal cycle of nonmigrating diurnal tides in the MLT region due to tropospheric heating rates from the NCEP/NCAR Reanalysis Project, *Adv. Space Res.*, *39*, 1347–1350, doi:10.1016/j.asr.2003.09.076.

Fritts, D. C., and M. J. Alexander (2003), Gravity wave dynamics and effects in the middle atmosphere, *Rev. Geophys.*, *41*(1), 1003, doi:10.1029/2001RG000106.

Fussen, D., et al. (2010), A global climatology of the mesospheric sodium layer from GOMOS data during the 2002–2008 period, *Atmos. Chem. Phys.*, *10*, 9225–9236, doi:10.5194/acp-10-9225-2010.

Garcia, R. R., D. R. Marsh, D. E. Kinnison, B. A. Boville, and F. Sassi (2007), Simulation of secular trends in the middle atmosphere, 1950–2003, *J. Geophys. Res.*, *112*, D09301, doi:10.1029/2006JD007485.

Gardner, C. S. (1989), Sodium resonance fluorescence lidar applications in atmospheric science and astronomy, *Proc. IEEE*, *77*, 408–418.

Gardner, C. S., and A. Z. Liu (2010), Wave-induced transport of atmospheric constituents and its effect on the mesospheric Na layer, *J. Geophys. Res.*, *115*, D20302, doi:10.1029/2010JD014140.

Gardner, C. S., D. G. Voelz, C. F. Sechrist Jr., and A. C. Segal (1986), Lidar studies of the nighttime sodium layer over Urbana, Illinois:

1. Seasonal and nocturnal variations, *J. Geophys. Res.*, *91*(A12), 13,659–13,673, doi:10.1029/JA091iA12p13659.

Gardner, C. S., J. M. C. Plane, W. Pan, T. Vondrak, B. J. Murray, and X. Chu (2005), Seasonal variations of the Na and Fe layers at the South Pole and their implications for the chemistry and general circulation of the polar mesosphere, *J. Geophys. Res.*, *110*, D10302, doi:10.1029/2004JD005670.

Gardner, C. S., X. Chu, P. J. Espy, J. M. C. Plane, D. R. Marsh, and D. Janches (2011), Seasonal variations of the mesospheric Fe layer at Rothera, Antarctica (67.5°S, 68.0°W), *J. Geophys. Res.*, *116*, D02304, doi:10.1029/2010JD014655.

Gardner, C. S., G. C. Papen, X. Chu, and W. Pan (2001), First lidar observations of middle atmosphere temperatures, Fe densities, and polar mesospheric clouds over the north and south poles, *Geophys. Res. Lett.*, *28*(7), 1199–1202, doi:10.1029/2000GL012622.

Grygalashvyly, M., E. Becker, and G. R. Sonnemann (2012), Gravity wave mixing and effective diffusivity for minor chemical constituents in the mesosphere/lower thermosphere, *Space Sci. Rev.*, *168*, 333–362, doi:10.1007/s11214-011-9857-x.

Grebowsky, J. M., and N. Reese (1989), Another look at equatorial metallic ions in the F region, *J. Geophys. Res.*, *94*(A5), 5427–5440, doi:10.1029/JA094iA05p05427.

Grebowsky, J. M., and A. Aikin (2002), In situ measurements of meteoric ions, in *Meteors in the Earth's Atmosphere*, edited by E. Murad and I. P. Williams, pp. 189–214, Cambridge Univ. Press, U.K.

Hastie, J. W. (1990), *Materials Chemistry at High Temperatures: Characterization*, 446 pp., Humana Press, New York.

Hedin, J., and J. Gumbel (2011), The global mesospheric sodium layer observed by Odin/OSIRIS in 2004–2009, *J. Atmos. Sol. Terr. Phys.*, *73*, 2221–2227.

Helmer, M., J. M. C. Plane, J. Qian, and C. S. Gardner (1998), A model of meteoric iron in the upper atmosphere, *J. Geophys. Res.*, *103*(D9), 10,913–10,925, doi:10.1029/97JD03075.

Hervig, M. E., L. G. Larry, M. R. James, and M. B. Scott (2009a), SOFIE PMC observations during the northern summer of 2007, *J. Atmos. Sol. Terr. Phys.*, *71*, 331–339.

Hervig, M. E., L. L. Gordley, L. E. Deaver, D. E. Siskind, M. H. Stevens, J. M. Russell III, S. M. Bailey, L. Megner, and C. G. Bardeen (2009b), First satellite observations of meteoric smoke in the middle atmosphere, *Geophys. Res. Lett.*, *36*, L18805, doi:10.1029/2009GL039737.

Höffner, J., and J. Lautenbach (2009), Daylight measurements of mesopause temperature and vertical wind with the mobile scanning iron lidar, *Opt. Lett.*, *34*, 1351–1353.

Hurrel, J. W., et al. (2013), The community earth system model: A framework for collaborative research, *Bull. Amer. Meteor. Soc.*, in press.

Janches, D., C. J. Heinselman, J. L. Chau, A. Chandran, and R. Woodman (2006), Modeling the global micrometeor input function in the upper atmosphere observed by high power and large aperture radars, *J. Geophys. Res.*, *111*, A07317, doi:10.1029/2006JA011628.

Jensen, D. E., and G. A. Jones (1974), Catalysis of radical recombination in flames by iron, *J. Chem. Phys.*, *60*, 3421–3425.

Kopp, E. (1984), Mesospheric H_2O and H_2O_2 densities inferred from in situ positive ion composition measurement, *Adv. Space Res.*, *4*(6), 13–18.

Kopp, E. (1997), On the abundance of metal ions in the lower ionosphere, *J. Geophys. Res.*, *102*(A5), 9667–9674.

Kopp, E., P. Eberhardt, U. Herrmann, and L. G. Björn (1985), Positive ion composition of the high-latitude summer *D* region with noctilucent clouds, *J. Geophys. Res.*, *90*, 13,041–13,053.

Lamarque, J.-F., et al. (2012), CAM-chem: Description and evaluation of interactive atmospheric chemistry in CESM, *Geosci. Model Dev.*, *5*, 369–411, doi:10.5194/gmd-5-369-2012.

Liu, A. Z. (2009), Estimate eddy diffusion coefficients from gravity wave vertical momentum and heat fluxes, *Geophys. Res. Lett.*, *36*, L08806, doi:10.1029/2009GL037495.

Liu, H.-L., et al. (2010), Thermosphere extension of the Whole Atmosphere Community Climate Model, *J. Geophys. Res.*, *115*, A12302, doi:10.1029/2010JA015586.

Lübken, F.-J., J. Höffner, T. P. Viehl, B. Kaifler, and R. J. Morris (2011), First measurements of thermal tides in the summer mesopause region at Antarctic latitudes, *Geophys. Res. Lett.*, *38*, L24806, doi:10.1029/2011GL050045.

Maitland, G. C., M. Rigby, E. B. Smith, and W. A. Wakeham (1987), *Intermolecular Forces: Their Origin and Determination*, Oxford Univ. Press, Oxford, U. K.

Marsh, D. R. (2011), Chemical-dynamical coupling in the mesosphere and lower thermosphere, in *Aeronomy of the Earth's Atmosphere and Ionosphere,* vol. 2, edited by M. A. Abdu and D.Pancheva, pp. 3–17, Springer, Netherlands, doi:10.1007/978-94-007-0326-1_1.

Marsh, D. R., R. R. Garcia, D. E. Kinnison, B. A. Boville, F. Sassi, S. C. Solomon, and K. Matthes (2007), Modeling the whole atmosphere response to solar cycle changes in radiative and geomagnetic forcing, *J. Geophys. Res.*, *112*, D23306, doi:10.1029/2006JD008306.

Marsh, D. R., M. Mills, D. Kinnison, J. Lamarque, N. Calvo, and L. Polvani (2013), Climate change from 1850 to 2005 simulated in CESM1(WACCM), *J. Clim.*, in press.

Merkel, A. W., D. R. Marsh, A. Gettelman, and E. J. Jensen (2009), On the relationship of polar mesospheric cloud ice water content, particle radius and mesospheric temperature and its use in multi-dimensional models, *Atmos. Chem. Phys.*, *9*, 8889–8901, doi:10.5194/acp-9-8889-2009.

Murad, E., and I. P. Williams (2002), *Meteors in the Earth's Atmosphere*, 322 pp., Cambridge Univ. Press, Cambridge, U. K.

Murray, B. J., and J. M. C. Plane (2003), The uptake of atomic oxygen on ice films: Implications for noctilucent clouds, *Phys. Chem. Chem. Phys.*, *5*, 4129–4138, doi:10.1039/b305555h.

Nahar, S. N., M. A. Bautista, and A. K. Pradhan (1997), Electron-ion recombination of neutral iron, *Astrophys. J.*, *479*, 497–503.

Pan, W., and C. S. Gardner (2003), Seasonal variations of the atmospheric temperature structure at South Pole, *J. Geophys. Res.*, *108*(D18), 4564, doi:10.1029/2002JD003217.

Pancheva, D., et al. (2002), Global-scale tidal structure in the mesosphere and lower thermosphere during the PSMOS campaign of June–August 1999 and comparisons with the global-scale wave model, *J. Atmos. Sol. Terr. Phys.*, *64*, 1011–1035.

Plane, J. M. C. (2002), Laboratory studies of meteoric metal chemistry, in *Meteors in the Earth's atmosphere*, edited by E. Murad and I. P. Williams, pp. 289–310, Cambridge Univ. Press, U.K.

Plane, J. M. C. (2003), Atmospheric chemistry of meteoric metals, *Chem. Rev.*, *103*, 4693–4984.

Plane, J. M. C. (2004), A time-resolved model of the mesospheric Na layer: Constraints on the meteor input function, *Atmos. Chem. Phys.*, *4*, 627–638, doi:10.5194/acp-4-627-2004.

Plane, J. M. C. (2012), Cosmic dust in the Earth's atmosphere, *Chem. Soc. Rev.*, *41*, 6507–6518, doi:10.1039/C2CS35132C.

Plane, J. M. C., R. M. Cox, and R. J. Rollason (1999), Metallic layers in the mesopause and lower thermosphere region, *Adv. Space Res.*, *24*(11), 1559–1570.

Plane, J. M. C., J. M. Murray, X. Chu, and C. S. Gardner (2004), Removal of meteoric iron on polar mesospheric clouds, *Science*, *304*, 426–428, doi:10.1126/science.1093236.

Plane, J. M. C., D. E. Self, T. Vondrak, and K. R. I. Woodcock (2003), Laboratory studies and modelling of mesospheric iron chemistry, *Adv. Space Res.*, *32*, 699–708, doi:10.1016/S0273-1177(03)00401-0.

Plane, J. M. C., and C. L. Whalley (2012), A new model for magnesium chemistry in the upper atmosphere, *J. Phys. Chem. A.*, *116*, 6240–6252.

Raizada, S., and C. A. Tepley (2003), Seasonal variation of mesospheric iron layers at Arecibo: First results from low-latitudes, *Geophys. Res. Lett.*, *30*(2), 1082, doi:10.1029/2002GL016537.

Rao, D. N., M. V. Ratnam, T. N. Rao, and S. V. B. Rao (2001), Seasonal variation of vertical eddy diffusivity in the troposphere, lower stratosphere and mesosphere over a tropical station, *Ann. Geophys.*, *19*, 975–984, doi:10.5194/angeo-19-975-2001.

Roddy, P. A., G. D. Earle, C. M. Swenson, C. G. Carlson, and T. W. Bullett (2004), Relative concentrations of molecular and metallic ions in midlatitude intermediate and sporadic-E layers, *Geophys. Res. Lett.*, *31*, L19807, doi:10.1029/2004GL020604.

Rollason, R. J., and J. M. C. Plane (1998), A study of the reactions of Fe^+ with O_3, O_2 and N_2, *J. Chem. Soc., Faraday Trans.*, *94*, 3067–3075, doi:10.1039/A805140B.

Rollason, R. J., and J. M. C. Plane (2000), The reactions of FeO with O_3, H_2, H_2O, O_2 and CO_2, *Phys. Chem. Chem. Phys.*, *2*, 2335–2343, doi:10.1039/B000877J.

Russell, J. M., III, M. G. Mlynczak, L. L. Gordley, J. Tansock, and R. Esplin (1999), An overview of the SABER experiment and preliminary calibration results, Int. Soc. for Opt. Eng., Denver, Colo., 18–23 July 1999.

Rutherford, J. A., and D. A. Vroom (1972), Formation of iron ions by charge transfer, *J. Chem. Phys.*, *57*, 3091, doi:10.1063/1.1678724.

Sakazaki, T., M. Fujiwara, X. Zhang, M. E. Hagan, and J. M. Forbes (2012), Diurnal tides from the troposphere to the lower mesosphere as deduced from TIMED/SABER satellite data and six global reanalysis data sets, *J. Geophys. Res.*, *117*, D13108, doi:10.1029/2011JD017117.

Saran, D. V., T. G. Slanger, W. Feng, and J. M. C. Plane (2011), FeO emission in the mesosphere: Detectability, diurnal behavior, and modeling, *J. Geophys. Res.*, *116*, D12303, doi:10.1029/2011JD015662.

Scharringhausen, M., A. C. Aikin, J. P. Burrows, and M. Sinnhuber (2008), Space-borne measurements of mesospheric magnesium species—A retrieval algorithm and preliminary profiles, *Atmos. Chem. Phys.*, *8*, 1963–1983, doi:10.5194/acp-8-1963-2008.

Self, D. E., and J. M. C. Plane (2002), Absolute photolysis cross-sections for $NaHCO_3$, NaOH, NaO, NaO_2, and NaO_3: Implications for sodium

chemistry in the upper mesosphere, *Phys. Chem. Chem. Phys.*, *4*, 16–23, doi:10.1039/B107078A.

Self, D. E., and J. M. C. Plane (2003), A kinetic study of the reactions of iron oxides and hydroxides relevant to the chemistry of iron in the upper mesosphere, *Phys. Chem. Chem. Phys.*, *5*, 1407–1418, doi:10.1039/B211900E.

Smith, A. K. (2012), Global dynamics of the MLT, *Surv. Geophys.*, *33*, 1177–1230, doi:10.1007/s10712-012-9196-9.

Singer, W., U. von Zahn, and J. Weiß (2004), Diurnal and annual variations of meteor rates at the arctic circle, *Atmos. Chem. Phys.*, *4*, 1355–1363, doi:10.5194/acp-4-1355-2004.

Swinbank, R., and D. A. Ortland (2003), Compilation of wind data for the Upper Atmosphere Research Satellite (UARS) Reference Atmosphere Project, *J. Geophys. Res.*, *108*(D19), 4615, doi:10.1029/2002JD003135.

Vondrak, T., J. M. C. Plane, S. L. Broadley, and D. Janches (2008), A chemical model of meteoric ablation, *Atmos. Chem. Phys.*, *8*, 7015–7031.

Vondrak, T., K. R. I. Woodcock, and J. M. C. Plane (2006), A kinetic study of the reactions of Fe^+ with N_2O, N_2, O_2, CO_2 and H_2O, and the ligand-switching reactions $Fe^+{\cdot}X + Y \rightarrow Fe^+{\cdot}Y + X$ ($X = N_2$, O_2, CO_2; $Y = O_2$, H_2O), *Phys. Chem. Chem. Phys.*, *8*, 503–512, doi:10.1039/B508922K.

Whiteway, J. A., and A. I. Carswell (1995), Lidar observations of gravity wave activity in the upper stratosphere over Toronto, *J. Geophys. Res.*, *100*(D7), 14,113–14,124, doi:10.1029/95JD00511.

Woodcock, K. R. S., T. Vondrak, S. R. Meech, and J. M. C. Plane (2006), A kinetic study of the reactions $FeO^+ + O$, $Fe^+{\cdot}N_2 + O$, $Fe^+{\cdot}O_2 + O$ and $FeO^+ + CO$: Implications for sporadic *E* layers in the upper atmosphere, *Phys. Chem. Chem. Phys.*, *8*, 1812–1821.

Yi, F., C. Yu, S. Zhang, X. Yue, Y. He, C. Huang, Y. Zhang, and K. Huang (2009), Seasonal variations of the nocturnal mesospheric Na and Fe layers at 30°N, *J. Geophys. Res.*, *114*, D01301, doi:10.1029/2008JD010344.

Yu, Z., X. Chu, W. Huang, W. Fong, and B. R. Roberts (2012), Diurnal variations of the Fe layer in the mesosphere and lower thermosphere: Four season variability and solar effects on the layer bottomside at McMurdo (77.8°S, 166.7°E), Antarctica, *J. Geophys. Res.*, *117*, D22303, doi:10.1029/2012JD018079.

Yue, X., Q. Zhou, S. Raizada, C. Tepley, and J. Friedman (2013), Relationship between mesospheric Na and Fe layers from simultaneous and common-volume lidar observations at Arecibo, *J. Geophys. Res. Atmos.*, *118*, 905–916, doi:10.1002/jgrd.50148.